scientific reports

Check for updates

OPEN

Hierarchical micro-nano topographies to control Bacteria and mesenchymal stem cells biological responses

M. T. Alameda[1,2]✉, M. R. Osorio[1], J. J. Hernández[1,3] & I. Rodríguez[1]✉

An ideal implant surface should promote cell attachment and tissue integration while preventing bacterial colonization. Engineering the surface topography of a biomaterial implant to elicit a differential response is a promising approach to dealing with both issues. To achieve this, we integrated Moth-Eye (ME) nanocones with micrometric features such as gratings and pillars in various hierarchical configurations, leading to different responses in bacteria and cells. These hierarchical topographies were tested on different polymers to compare their biological responses. Mesenchymal stem cells (MSCs) were employed as a model system to study cell behavior, given their ability to proliferate, self-renew, and differentiate. The bactericidal effect was tested using gram-negative *Escherichia coli* and gram-positive *Staphylococcus aureus*. Results show that these topographies-maintained cell viability and influenced cell morphology, orientation, migration and differentiation, which are crucial processes for regeneration and osseointegration. Finite Element Method (FEM) simulations estimated the traction forces generated by cells on these surfaces. Overall, the hierarchical topographies enhanced the expression of osteogenic markers in the MSCs while retaining the bactericidal properties of the ME nanostructures.

Keywords Hierarchical topography, Nanostructures, Mechano-bactericidal, Mechanosensing, Differentiation, Osteogenesis, Cell-instructive, FEM

Due to increased life expectancy and an ageing population, there is a growing demand for prosthetic implants to restore or regenerate the lost normal function of a body part[1,2]. However, implant fixation and functional recovery of the lost function do not always occur, with the most frequent failures being the lack of biointegration in the host tissue and bacteria proliferation on the surface of the implant. In these processes, the characteristics of the implant surface play a critical role for proper implant integration with tissues[3–6]. The introduction of a foreign body automatically triggers an inflammatory response, while bacteria, if present, would initiate the so-called "race for the surface" with the host cells to colonize the surface of the implant. The latter process was first described in 1988 by Gristina et al., who recognized that the outcome of this competition dictates the success of an implant biointegration[7]. When bacteria adhere to an implant's surface and form a biofilm, they become highly resistant to bactericidal agents. The implant surface acts as a shield against the immune system, creating a conducive environment for infection. As a result, implant infections often lead to implant failure and removal becomes necessary. Systemic antibiotics are routinely prescribed in patients undergoing implantation surgeries to prevent early implant failure. Nevertheless, implant-related infections still occur in approximately 5% of orthopedic implant procedures[8]. In addition, this routine and the widespread use of antibiotics is driving the emergence of antibiotic-resistant bacteria strains[9–11].

Research has shown that the surface texture of an implant significantly affects its ability to integrate into biological tissues. In this regard, micro- and nano-engineering offers an opportunity to create micro- and nanotopographical surface features that can influence cellular responses. Indeed, extensive research has consistently demonstrated that surface topography is crucial in guiding cellular behavior and fate, influencing aspects such as cell morphology, adhesion, proliferation/viability, migration, and differentiation[12–15]. These

[1]Madrid Institute for Advanced Studies in Nanoscience (IMDEA Nanociencia), Ciudad Universitária de Cantoblanco, C/Faraday 9, Madrid 28049, Spain. [2]Centro Singular de Investigación en Química Biolóxica e Materiais Moleculares (CiQUS), Departamento de Química Inorgánica, Universidade de Santiago de Compostela, Santiago de Compostela 15782, Spain. [3]Present address: Instituto de Estructura de la Materia (IEM), CSIC, Serrano 121, 28006 Madrid, Spain. ✉email: mariateresa.alameda@imdea.org; i.rodriguez@imdea.org

responses have been shown to occur through the modulation of focal adhesions (FAs) influenced by surface topography, which activates various downstream cell signaling pathways[16–20]. FAs are protein complexes that assemble through integrin transmembrane receptors to the external environment, transducing bidirectional mechanical forces into the cell and vice versa, inducing cell cytoskeleton reorganization[21]. These biomechanical responses are influenced not only by topographical cues, but also by the mechanical properties of the surface. Particularly, substrate stiffness has been shown to affect fundamental cellular processes, including spreading, proliferation, migration, differentiation and tumoral progression[22–25]. Hence, many works have focused on understanding the response of stem cells to different mechanical cues[26,27]. Studies on Mesenchymal Stem Cells (MSCs) are particularly interesting, as these cells are involved in wound healing and regeneration processes by coordinating repair at different levels of response, i.e., through differentiation, immunomodulation, and secretion of growth factors[28,29]. Some earlier works have recognized the ability of nanotopographies to influence the MSCs differentiation towards the osteocyte lineage. Conversely, other studies have highlighted their capacity to maintain a long-term stemness, preserving the cell's capacity for self-renewal[30–32].

As previously stated, it is essential to prevent infection of the implant surface to ensure proper implant biointegration. To this end, nanostructured materials have emerged as an attractive strategy to deter bacterial attachment and proliferation through mechano-bactericidal effects. In recent decades, different nanotopographies, many of them bioinspired by natural sources, have been shown to offer protection against bacteria[10,33]. For example, lotus leaves and butterfly wing nanostructures possess self-cleaning properties, which may prevent bacterial attachment due to their powerful superhydrophobicity repelling water droplets[34–36]. Other species such as cicadas and dragonfly wings or moth-eyes (MEs)[37–41], have developed nanostructures to prevent bacterial infection by mechanical stress and deformation of the bacteria cell envelope upon attachment to the surface compromising the viability of the bacteria[42,43].

Only a limited number of studies have addressed the problem of implant biointegration from a both host cell biointegration and bacterial infection perspectives. Among these, few have approached the issue from a physical standpoint, specifically through topographical modifications of the material[37,44,45].

Here, we propose a hierarchical micro-nano topography for directing the behavior of MSCs while preventing bacteria colonization. The hierarchical topography consists of a micrometric arrangement covered by a nanometric texture. The dimensions of the micro- and nanofeatures were chosen based on previous works. The micro features were intended to instruct the response of MSCs[46]. Several microtopographies have been assessed with an aspect ratio of 1:2 (height: diameter), an interspace of 2 µm, and varying degrees of anisotropy. Previous nanotopographies with bactericidal action have involved surface features in the range of 10–100 nm at the contact point to generate a bactericidal effect[14,42,47]. In this work, for the hierarchical topography, we selected the bioinspired ME nanocones because of their known bactericidal effect and proven cytocompatibility[37]. The ME nanofeatures were implemented on the upper and lower levels of the microtopography covering the entire surface. The materials selected to fabricate the topographies in comparative studies were polydimethylsiloxane (PDMS) in hard and soft variations (hPDMS and sPDMS respectively) and poly(methyl methacrylate) (PMMA), both polymers commonly used in implants. MSCs were cultured on these substrates to assess the changes in cell viability, morphology, motility, and differentiation –specifically towards the osteogenic lineage– induced by the topographies. Finite Element Method (FEM) simulations were conducted to substantiate how the mechanical properties of the substrates affect the response of the MSCs by investigating cell traction forces in relation to the stiffness of the topography. Likewise, the bactericidal efficacy of these topographies was evaluated for *E. coli* (gram-negative) and *S. aureus* (gram-positive) strains. The results suggest that hierarchical topographies could be an effective tool for directing the biological response of MSCs while preventing bacterial infection, both important processes in reducing implant failure.

Results and discussion

Substrate fabrication and characterization

A range of micro- and nanostructured surfaces and hierarchical arrangements on various polymeric materials, including the elastomeric polydimethylsiloxane polymer (PDMS) or thermoplastic poly(methyl methacrylate) (PMMA), were fabricated with the aim of eliciting distinct responses in mammalian cells and bacteria. Figure 1 shows representative SEM images of the different topographies examined in this study. These topographies, classified into three main categories include: (1) Nanotopography, consisting solely of Moth-Eye nanocones (ME); (2) Microtopographies, which include both Low Aspect Ratio (LAR) and High Aspect Ratio (HAR) features such as Gratings, Square Pillar Arrangement (SPA), and Hexagonal Pillar Arragement (HPA); and (3) Hierarchies, combining LAR microtopographies with ME nanocones (LAR + ME). The geometrical details are summarized in Table S1 of the Supplementary Information.

Initially, the wetting properties of the different fabricated substrates were evaluated by measuring the water contact angle (WCA) on each surface. A summary of the data obtained is displayed in Fig. 2(a). The analysis of the WCAs indicates that the nano- and microtextured substrates increased their hydrophobicity compared to their flat counterparts. Moreover, all the topographic substrates were more hydrophobic than the standard cell culture plates, which were used as a reference control (labelled as PS flat). On the grating topographies, two different WCA values were obtained due to the anisotropic spreading of water droplets in the direction of the grating.

The wettability of the substrates after exposure to the culture medium was also investigated. To do so, the ME nanopatterned hPDMS and PMMA substrates were incubated in a protein-enriched culture medium such as Luria-Bertani (LB) broth for 5 h. The results obtained displayed in Fig. 2(b) indicate that after the incubation period, all substrates become highly hydrophilic with WCA values below 50. This was an expected result caused by the adsorption of proteins in the medium thereby changing the surface chemistry and charge. This is an

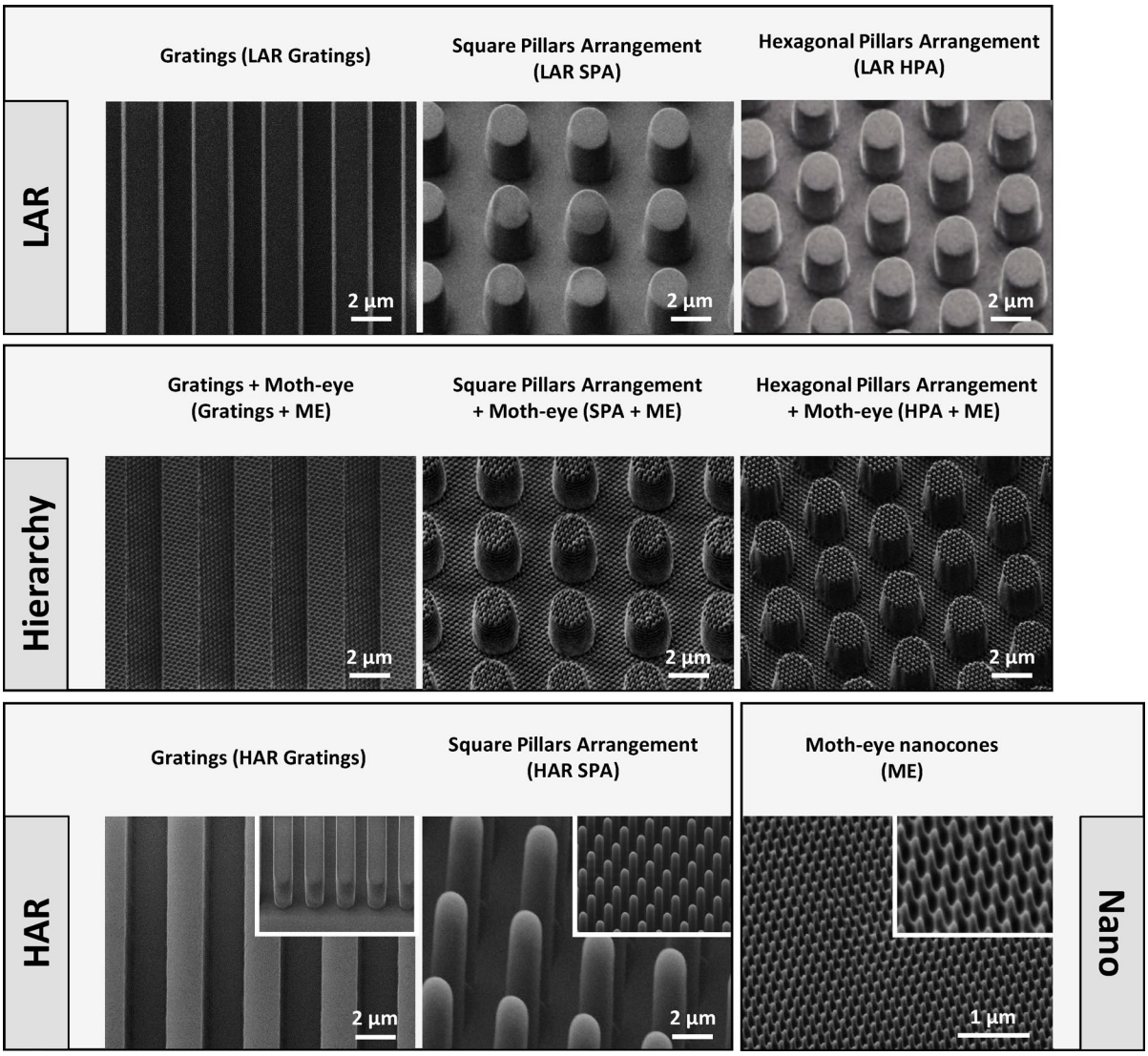

Fig. 1. SEM images of the different topographies under study fabricated in (polydimethyl siloxane) PDMS and (poly(methyl methacrylate)) PMMA. The topographies are classified according to their aspect ratio as LAR (Low Aspect Ratio), HAR (High Aspect Ratio) microtopographies and ME (Moth-eye) nanocones. The hierarchical topographies include a combination of the LAR features with ME nanocones. The geometrical arrangements are either HPA (Hexagonal Pillar Arrangement), SPA (Square Pillar Arrangement) and Gratings.

event that takes place naturally when a biomaterial surface comes in contact with biological fluids, forming a conditioning layer that influences subsequent cellular attachment and biomaterial integration[48].

Given that oxygen plasma is a standard surface treatment for conventional polystyrene culture plates, we also investigated the changes in the WCA of our topographies following this treatment[49–51]. Figure 2(c) displays the WCAs for the ME topography fabricated in hPDMS and its flat counterpart after treatment with oxygen plasma. It can also be seen that after periods of 1 h, 24 h and 72 h post-treatment, the surface activation was not stable over time, as the wetting behavior of the surface gradually reverted when the substrates were stored in air. This result indicates that cell culture substrates should be promptly pre-incubated in the corresponding medium following plasma activation to enhance protein adsorption, thereby optimizing conditions for cellular adhesion and growth.

Cell proliferation

Cell proliferation was assessed by the resazurin assay. The proliferation of MSCs on the different topographic substrates (ME, LAR, HAR and hierarchies) was compared to that of their respective PS flat controls. Before cell culture, the surfaces were pretreated with oxygen plasma to favor wetting in culture medium and cell adhesion. The proliferation curves obtained are displayed in Fig. 3. As can be seen, all the substrates supported the growth of the MSCs. However, unlike the PS flat control, which exhibited a steady increase in proliferative activity, the proliferation rate on the topographies was somewhat slower during the initial days. This occurrence was previously reported, and it has been associated with a slowdown in cell cycle progression. The underlying

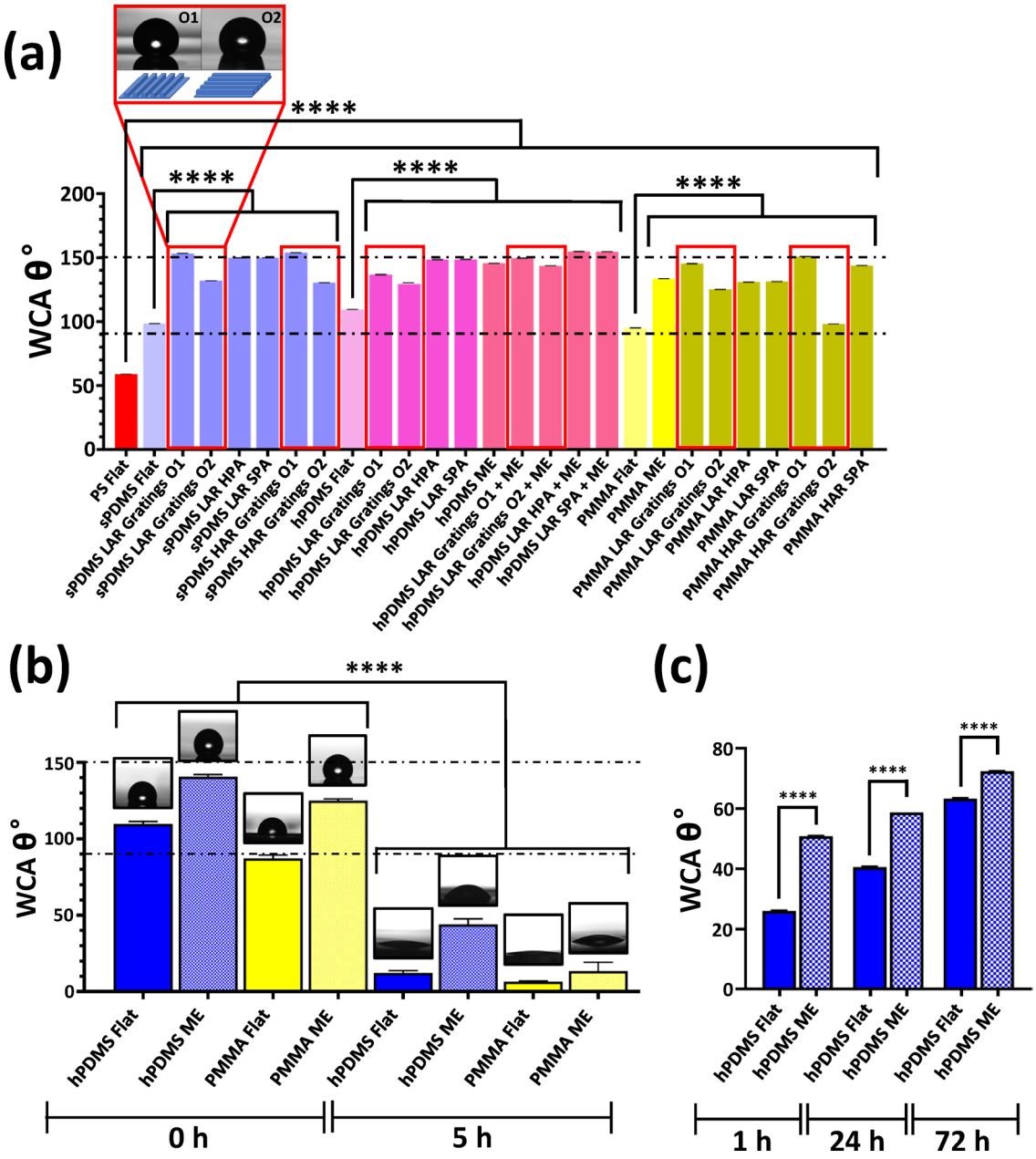

Fig. 2. Wetting properties of the topographies used for the study. **(a)** WCAs measured on sPDMS, hPDMS, and PMMA substrates with a wide variety of topographies (nano-, hierarchical (LAR + ME), LAR and HAR microtopographies). Note the difference in the WCA of the gratings according to their orientation (shown by red box, O1 and O2). **(b)** WCAs measured in flat and ME nanopatterned substrates fabricated on hPDMS and PMMA polymers before and after 5 h incubation in a protein-enriched medium (LB broth). **(c)** WCAs for hPDMS either flat or topographed (ME) at 1 h, 24 h and 72 h after oxygen plasma treatment. Measurements were plotted as the WCA mean ± SE. One-way ANOVA analysis shows statistical significance by **** p-value < 0.0001. Dashed lines show the contact angle intervals that determine hydrophilicity ($\theta < 90^\circ$), hydrophobicity ($90^\circ < \theta < 150^\circ$) and superhydrophobicity ($150^\circ < \theta$). Representative water droplets are shown above data columns.

mechanism involves mechanobiological signaling pathways regulated by cytoskeletal reorganization, which is itself modulated by the structural properties of the surface[52]. Conversely, when comparing only flat surfaces to evaluate the effect of material stiffness, it was observed that increased stiffness corresponded with greater cell proliferation. This outcome agrees with earlier reports, where MSCs exhibited lower proliferation on PDMS than on PS tissue culture plates[53]. Nonetheless, around the 4th −5th day, an increase in the proliferative behavior of the MSCs was observed on the nano- and microtopographies. Attending only to flat surfaces, sPDMS exhibited the lowest proliferation rate (Fig. 3(d)) whereas the topographies in this material showed significant variations

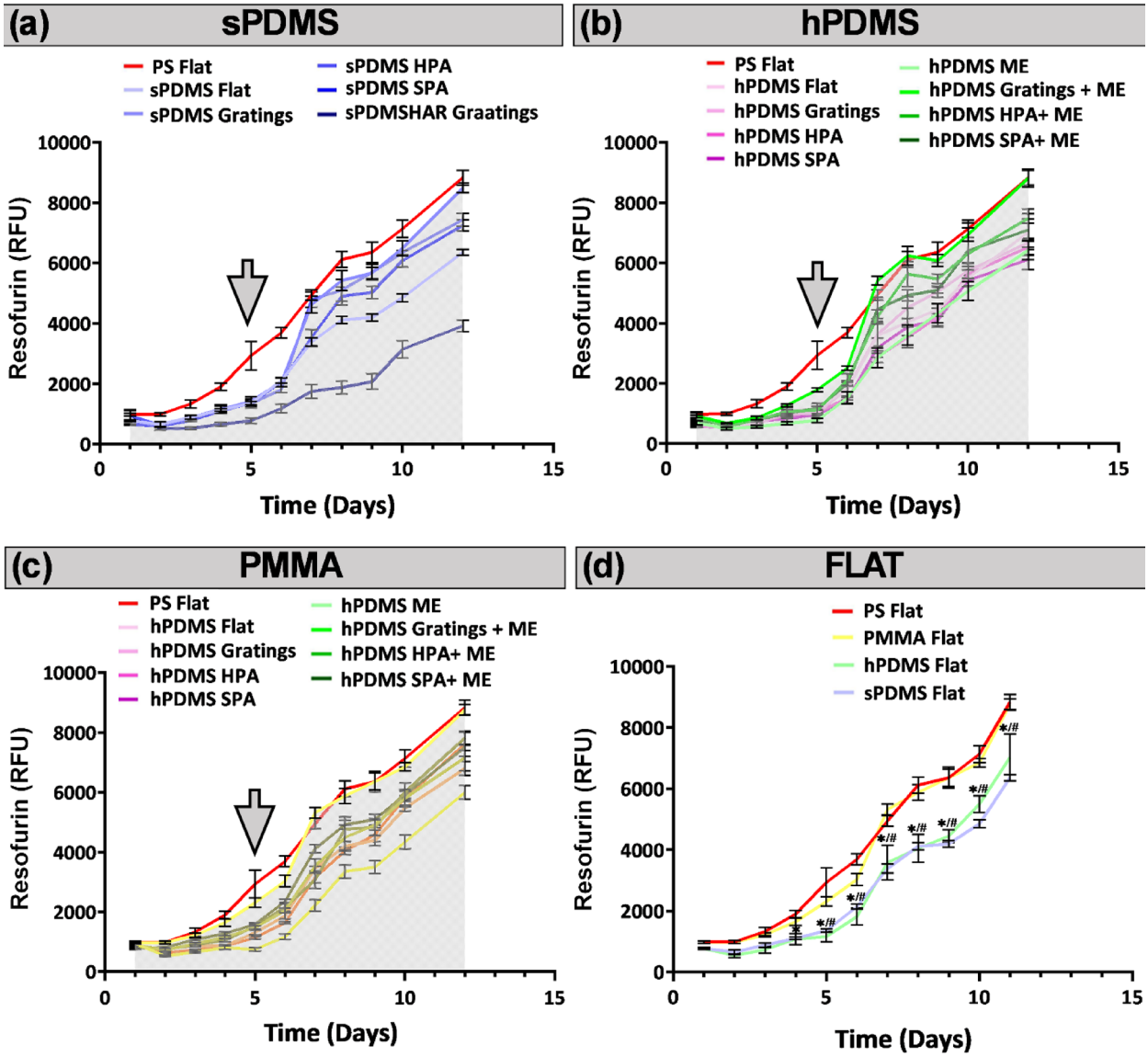

Fig. 3. Cell proliferation dynamics of MSCs –measured as resofurin fluorescence intensity (Ex. 550/Em. 590 nm; mean ± SE) were analyzed to assess the growth of MSCs. MSCs cultured on different substrates (ME, LAR, HAR, hierarchies (LAR + ME)) made in three different materials: **(a)** sPDMS, **(b)** hPDMS, and **(c)** PMMA. **(d)** MSCs cultured on flat sPDMS, hPDMS, and PMMA polymers. One-way ANOVA test followed by Holm-Šídák post-hoc analysis was carried out for comparing the MSCs proliferation rates between polymers at each time point. Significant differences are marked by */# ($p < 0.05$) for both sPDMS and hPDMS respectively. PS flat substrate from tissue-culture plates was included as a control. Gray shading highlights the top-performing conditions, emphasizing the early-culture response (days 4–5), where the highest growth increment occurs relative to the PS control (threshold reference). Gray arrows denote the phase of maximal proliferation increase.

in proliferation rates (compare the length of the red arrows in Figs. 3(a), with 3(b) and 3(c)). This could be attributed to the fact that sPDMS is the softest polymer among the substrates tested.

Both wettability and cell proliferation assays indicated that an oxygen-plasma pretreatment adequately sustained cell growth on the surfaces[54,55]. Hence, for subsequent studies, all surfaces were pre-treated with oxygen plasma under the same conditions prior to incubation with the cell medium.

Morphological cell response

Topographical and mechanical characteristics of substrates have been shown to influence cell shape and spreading through mechanotransduction processes, shaping cellular behavior as they interact with their surroundings[56,57]. Images of MSCs cultured on the different substrates with cytoskeleton and nuclei fluorescently labelled were analyzed to characterize the cell morphology adopted on the different topographies. The morphological parameters analyzed (area, circularity, eccentricity, and orientation) were performed with CellProfiler software,

establishing a correspondence of cell nuclei with the cytoskeleton as illustrated in Figure S1(a) from the Supplementary Information. Figure S1(b) shows some representative post-processed images of each data set analyzed.

Figure 4(a) depicts the cell projected area measurements for the MSCs cultured on LAR topographies fabricated on the different materials. Here, the largest mean area values were observed for cells cultured over the hPDMS substrates in all the topographies. Figure 4(b) shows representative images comparing the cell area outlined by a green line between the different materials tested patterned with the LAR HPA topography. In turn,

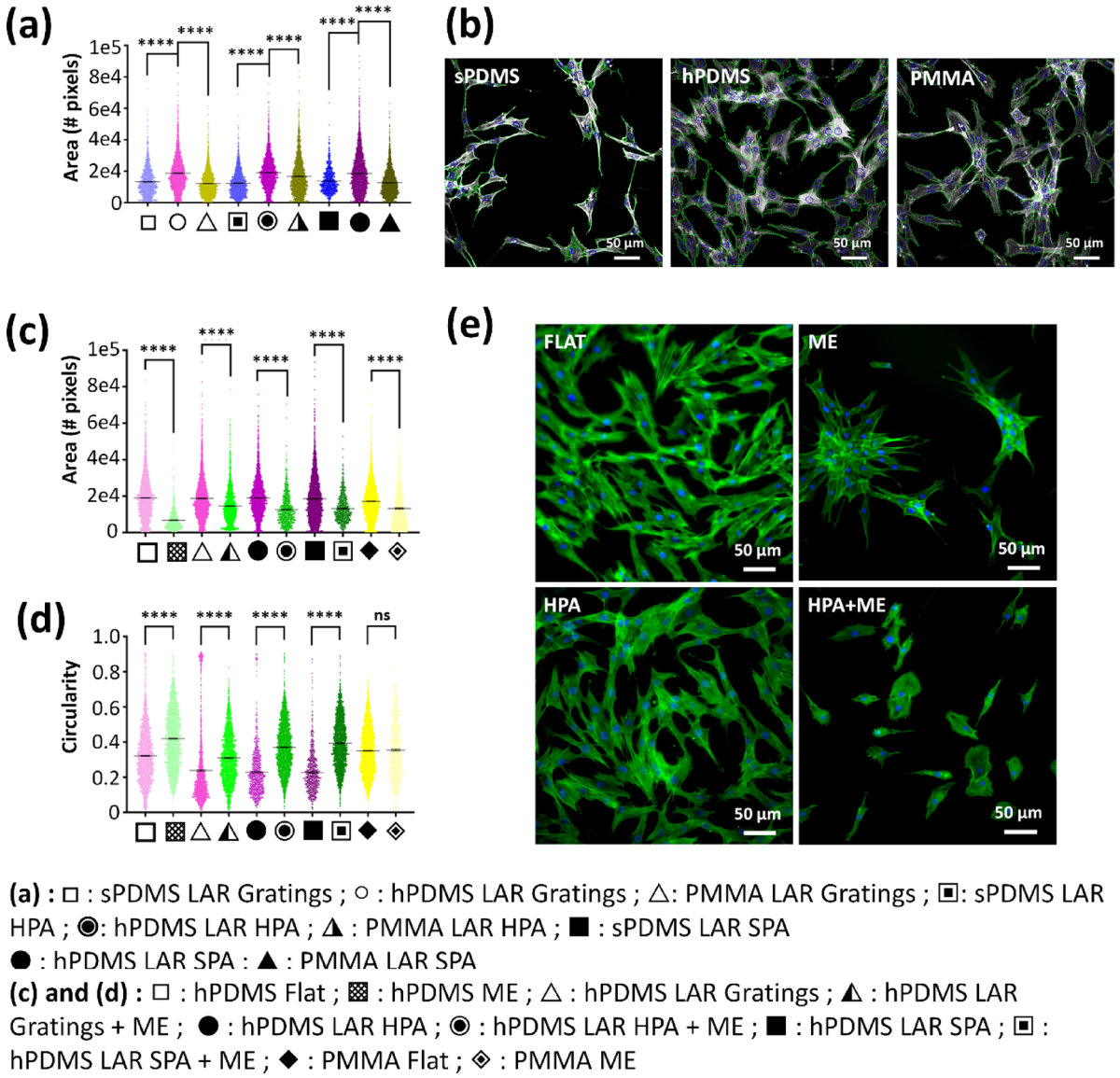

Fig. 4. **(a)** Influence of the substrate polymeric material over the cell area (mean ± SE) of MSCs, showing the comparison between different materials (sPDMS, hPDMS, and PMMA) with the same microtopography. The projected cell area is outlined in green for each cell, with the nucleus identified by a blue outline. **(b)** Representative images comparing the cell area of MSCs across various materials patterned with the LAR HPA topography. The outlines of the cytoskeleton and nucleus are shown in green and blue lines, respectively. **(c)** Influence of the ME nanostructure on MSC cell area (mean ± SE) . For each substrate, it is shown the comparison with its non-ME counterpart. **(d)** Influence of ME nanostructure over circularity (mean ± SE) for MSCs cultured onto different substrates, compared with the non-ME counterparts. **(e)** MSCs actin and nucleus staining grown onto different substrates. Representative pictures exemplify the influence of the ME nanostructures comparing hPDMS Flat vs. ME and hPDMS HPA vs. HPA + ME (hierarchy). Upper row shows the influence of the nanostructure compared to a flat substrate, while the bottom row shows this influence for a substrate that includes a microtopography, as in this case, HPA. One-way ANOVA statistical analysis was performed for comparisons. Significance is displayed by ns (not significant) and * symbols (ns $p > 0.05$, * $p < 0.05$, ** $p < 0.01$, *** $p < 0.0001$, **** $p < 0.0001$).

each cell is identified by its respective nucleus outlined by a blue line. This behavior was also observed on flat surfaces, where there is no influence from topography (see also in Figure S2(a)).

Notably, substrates patterned with the ME nanostructure, including hierarchical features, significantly reduced the cell projected area, regardless of the material (see Fig. 4(c)). In terms of cell circularity, the presence of ME nanostructure was also found to induce a more isotropic rounded cell shape, as it can be seen in Fig. 4(d). Figure 4(e) presents fluorescence images of MSCs illustrative of the impact of the ME nanostructures on the cellular shape compared to a flat substrate (upper row) and the LAR HPA hierarchical arrangement (lower row) compared with their control without ME nanostructures. Thus, the presence of ME nanostructures not only decreased cell area but also increased circularity. These findings further confirm that the spatial constraints imposed by nanopatterning influenced cell spreading[58].

Another remarkable effect in terms of cell shape is that for the MSCs cultured on more anisotropic topographies, such as LAR gratings, typically a more elongated shape was observed (see Figure S2(b)). Conversely, stiffness not only affected elongation but also influenced cell shape by preventing the typical circularity observed in anisotropic topographies. In this case, the effect of anisotropy is overshadowed by the stiffness effect on the PMMA substrates, where higher mean values of cell circularity were seen (see Figures S2(c) and S2(d)).

The orientation of cells was evaluated based on their angular distribution across the topography, indicating the primary direction that cells adopt when growing on these surfaces. The orientation of cells was evaluated based on their angular distribution across the topography, indicating the primary direction that cells adopt when growing on the topographies. The rose plots in Fig. 5(a) depict the mean cell orientation adopted by MSCs cultured in substrates with features of increasing anisotropy. The mean resultant vector, represented as the R value (displayed by a red line in the rose plots), increased as the substrate became more anisotropic reaching a maximum value for gratings. Conversely, in more isotropic topographies such as flat surfaces or HPA, the cells were more randomly distributed and low R values were observed. The SPA substrates, with an intermediate degree of anisotropy, did not induce any statistically predominant orientation, thus, medium-low values for the length of the mean resultant vector were obtained. These findings suggest that cells align with the grating topographic structure, demonstrating a directional organization that is consistent with observations reported in previous studies[59–61]. Figure 5(b) shows a comparison of the R value obtained in relation to the substrate topographic feature. The figure signifies that the highly anisotropic grating results in high R values, attributed to the predominant orientation adopted by the cells.

Cell orientation was also influenced by the aspect ratio of the microstructure for the stiffer materials. This cell alignment effect was noticeable when comparing the HAR PMMA gratings with their LAR counterparts (see Figure S3(a)). On the other hand, results show that the ME nanostructure does not affect cell orientation when it is part of a hierarchical topography (see Figure S3(b)). This result is expected since an isotropic hexagonal arrangement such as the ME nanostructure should not promote any particular orientation. Even when patterned over anisotropic microstructures, the ME topography did not alter cell orientation distribution when compared with the non-hierarchical counterpart. On the other hand, the star-like clustering of MSCs on the ME nanotopogarphy was noteworthy (see upper-right row from Fig. 4(e)). This behavior has previously been observed on uncoated and non-nanostructured PDMS substrates[53,62]. Our findings indicate that this clustering effect is mostly driven by the ME nanotopography regardless of the material, either PDMS or PMMA. The organization of cells into clusters is relevant for constructing functional microtissues, as it promotes stable cellular networks and extracellular matrix production, which are essential steps for effective integration with host tissues[63,64].

Cell migration behavior

The characterization of cell migration behavior on a surface topography is important to predict the ability of the host cells to migrate and attach to the implant surface, facilitating osseointegration. The motility of the MSCs cultured on different substrates was measured by the cell average speed calculated from the time-lapse images of the cell trajectories. The results are displayed in Fig. 6. The results in Fig. 6(a) indicate that stiffness of the substrate significantly influenced the cell motility. The data indicate that cell motility was highest on substrates with intermediate stiffness (see Table 1 from Methods: hPDMS $E \sim 9$ MPa), whereas it decreased on both softer and stiffer materials. Indeed, cell motility is directly linked to the turnover rate of focal adhesions (FAs), which is modulated by the stiffness of the substrate. On stiffer materials, an enhanced cell attachment prevents the rapid disassembly of FAs in the rear edge of the cell, delaying cellular migration. On the contrary, softer materials preclude the formation of stable FAs in the front edge, which also limits FA turnover. This biphasic behavior of cell motility, where cells exhibit optimal migration speeds at intermediate substrate stiffness, has been described in previous studies. This behavior is influence by the turnover rate of FAs in response to material stiffness[65–67].

Patterning of the surfaces had also an influence on cell adhesion and motility. Figure 6(b) shows that for the same microtopography, the average cell migration speed decreased on the hPDMS substrates while it increased in sPDMS. On these substrates, the stiffness-dependent biphasic behavior of cell motility appeared to be modulated by the substrate microtopography. However, no significant differences were observed when comparing different microstructures fabricated in the same polymeric material. This indicates that the stiffness of the material has a greater influence on cell migration speed than the spatial distribution of the topographic features. Nevertheless, it is well-documented that cells modulate their migration behavior in response to different topographic features[68].

Our observations further demonstrated that nanotopographical features within the hierarchical surface influenced cell motility. Figure6(c) shows that the ME nanocones increased the average cell speed compared to the micro topographies not including the ME substrates. Previous studies have shown that nanosized features can hinder the formation of large, mature FAs by restricting integrin clustering. The dimensional constrains imposed by these features limit the available area for integrin clustering, thereby hindering the maturation

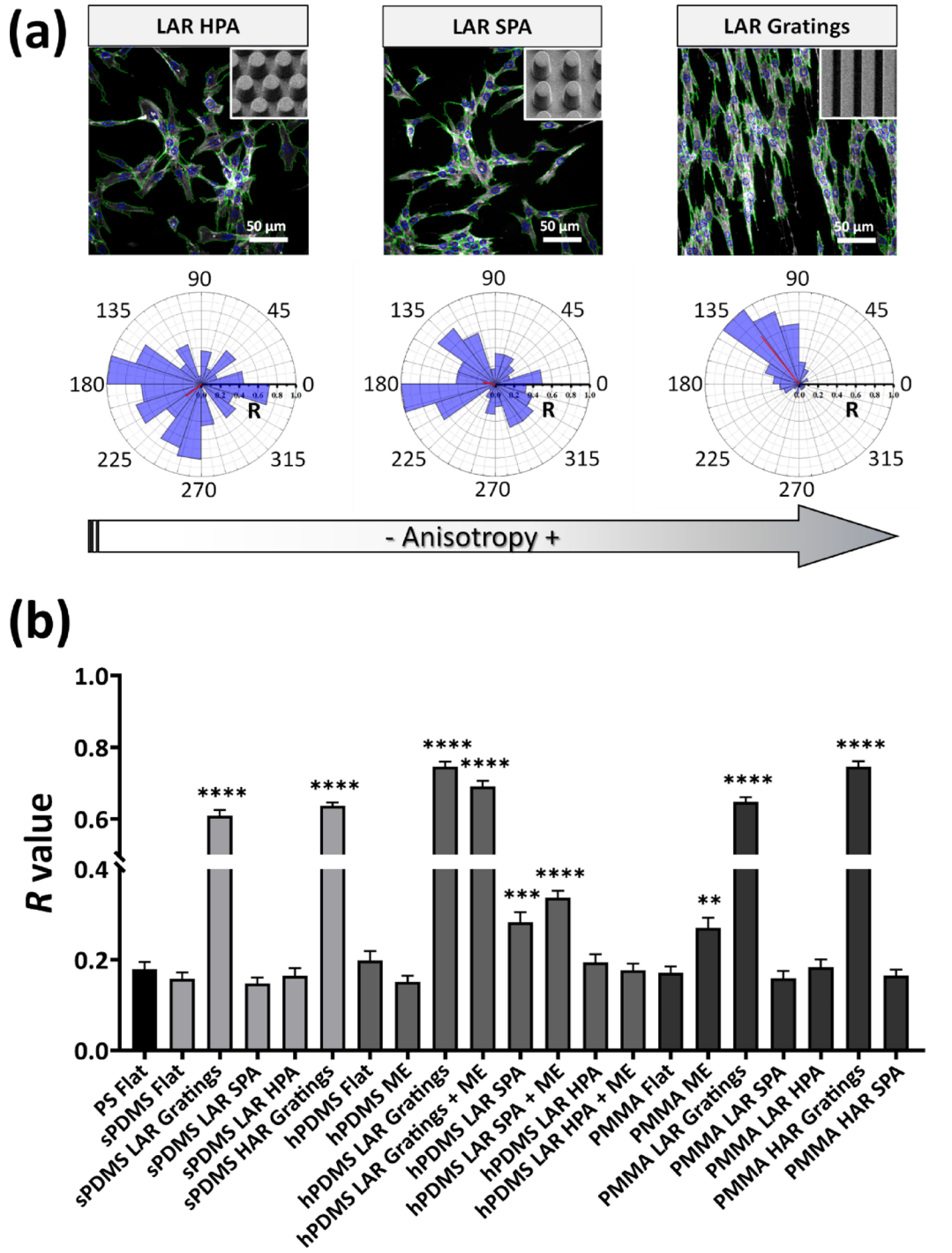

Fig. 5. One-way ANOVA analysis followed by Holm-Šídák post-hoc test comparing the length of the mean resultant vector, *R* , which represents the directionality degree acquired by MSCs cultured on the different substrates. Significant data is established by asterisks (* $p < 0.05$, ** $p < 0.01$, *** $p < 0.001$, **** $p < 0.0001$) and non-significant (ns) for the corresponding comparisons. **(a)** Representative fluorescence images of cells grown in the three main geometric arrangements analyzed (Gratings, SPA, HPA) -exemplified by the PMMA substrate- and their respective rose diagrams below show their angular distribution (violet facets) and their main acquired orientation (*R* values shown by the red line). **(b)** The plot shows a comparison between the flat PS control and the different substrates studied. The high *R* values ($R > 0.6$) are noteworthy for the most anisotropic topographies, whichexhibited particularly significant differences.

process of FAs[58,69]. Accordingly, our findings suggest that the ME nanostructures did not facilitate integrin clustering, which in turn, led to a rapid FA turnover, ultimately enabling a faster rate of cell migration[70,71].

The aspect ratio of the microstructures was also seen to influence the average cell migration speed as seen in Fig. 6(d). The more flexible HAR microfeatures were found to be less conducive to rapid cell migration compared to the LAR ones. This result is consistent with previous findings, showing that cells on HAR topographies exhibited reduced motility while experiencing increased cell traction forces[14].

The influence of topographic anisotropy on the cell migration directionality was also investigated. Figure 6(e) shows the directionality of cell migration observed in gratings (anisotropic) comparatively to HPA (isotropic). It can be seen that, the degree of anisotropy played a crucial role in guiding the directional migration of cells, following the same tendency seen in studies on cell spreading (see rose plots in Fig. 5(a)). The graph highlights the significant effect of the more anisotropic topographies notably influencing the cell movement, guiding it to become directional and persistent. On the other hand, the aspect ratio of the microstructure exhibited minimal influence on cell migration directionality.

The persistence of cell migration was estimated based on the cellular trajectories obtained from cell tracking video images (see Video S1 in Supplementary Information). From these videos, the α-values were calculated to quantify the persistence of the cell migrating path. Figure 6(f) displays the comparison between the different topographies in hPDMS. An increase in the α-value can be observed on the topographies with higher anisotropy (i.e., gratings and SPA). The increase in migration speed was most pronounced when comparing the grating topography to other microtopographies fabricated in hPDMS (Figure S4). This effect correlated with the optimal substrate stiffness for promoting cell motility among all tested polymer materials. Conversely, the addition of the ME topography to these microtopographies systematically induced greater migration randomness (lower α-value) as it can also be seen in Fig. 6(f). Moreover, the influence of anisotropy on the persistence of cell migration became more evident as the aspect ratio increased (see Fig. 6(g)) in agreement with previous works[72,73].

Cell traction forces: simulation vs. experiments

We employed Finite Element Method (FEM) simulations to examine how forces exerted on the different topographies, led to a different degree of deflection and von Mises stress distribution depending on material stiffness. These simulation results were compared with the deflections caused by the cellular tractions on the polymeric topographies and observed experimentally by SEM. Figure 7 shows representative examples of these for four different substrates: sPDMS + hPDMS hierarchical LAR pillars (Fig. 7(a)), sPDMS LAR pillars (Fig. 7(b)), sPDMS HAR gratings (Fig. 7(c)), and HAR micropillars (Fig. 7(d)). The complete set of simulations is also shown in Figure S5 as Supplementary Information. Our study examined the mechanical deformation of topographic features under cell traction forces on LAR and HAR microtopographies with two different geometries (SPA and gratings) fabricated on sPDMS, hPDMS, and PMMA polymers. In these simulations, only the forces applied at the at the upper part of the topographic features were considered as these are the areas where FAs predominantly form[19]. These simulations allow for the observation of the microstructure's degree of deflection and the von Mises stress distribution onto the underlying substrate and adjacent microfeatures. Their magnitude is influenced by both the stiffness of the substrate and the geometric characteristics of the topography. The deflection or deformation of topographical features is determined by the ratio between the applied forces to Young's modulus. That is, softer materials require less force to achieve significant displacements, whereas stiffer materials approach a deflection saturation point only at higher force values[74–77]. The simulations also showed that the aspect ratio plays a critical role in the mechanical behavior of topographical features with higher aspect ratios leading to increased deflection and Von Mises stress in response to traction forces. As the SEM micrograph shows in Fig. 7(d), even HAR micropillars of PMMA, the stiffest among the tested polymers, bend under cell traction forces when the aspect ratio is high enough, i.e., aspect ratio = 5.

As the SEM micrograph shows in Fig. 7(d), even HAR micropillars of PMMA, the stiffest among the tested polymers, bend under cell traction forces when the aspect ratio is high enough, i.e., aspect ratio = 5.

Hierarchies that include the material combination sPDMS + hPDMS were also studied. The importance of the contribution of the different polymeric layers, either hPDMS from the top or sPDMS from the base of the pillar to the stiffness in the hierarchical topographies was simulated. As shown in Fig. 7(a), the two polymeric layers influenced the mechanical properties of the topography, as evidenced by the bending of the pillar under cell traction forces, with a deflection length falling between those observed for sPDMS and hPDMS (see Figure S6).

Differentiation into osteocyte lineage

The extent of osteogenic differentiation of MSCs cultured on different topographical and polymeric substrates was investigated under inductive differentiation conditions. Alizarin Red S was initially used to stain calcium deposits generated by the mineralization process taking place during osteogenesis. This assay served to determine the optimal incubation time (14–21 days of osteogenic induction) for detecting the differentiation of MSCs into the osteocyte lineage. Based on the results, the differentiation of MSCs on the different topographies was studied after 21 days of culture under osteogenic inductive conditions by evaluating the expression of specific osteoblastic biomarkers (OCN, OPN). The entire set of representative images obtained in the Alizarin Red S and specific osteogenic biomarker experiments with their corresponding analyses can be seen in Figures S7, and in Figures S8 and S9 respectively in the Supplementary Information.

The Alizarin Red S test results, depicted in Fig. 8(a), evidence the effect of stiffness in cell differentiation, which takes place earlier on the stiffest PMMA substrate compared to the other softer materials. In the PMMA substrates, calcium deposits-stained red are already noticeable at 14 days as contrasted with soft substrates, which are even more marked after 21 days under inductive conditions. These findings are consistent with previous works, in which stiffness was seen as a key parameter to promote osteogenic differentiation[56,78,79].

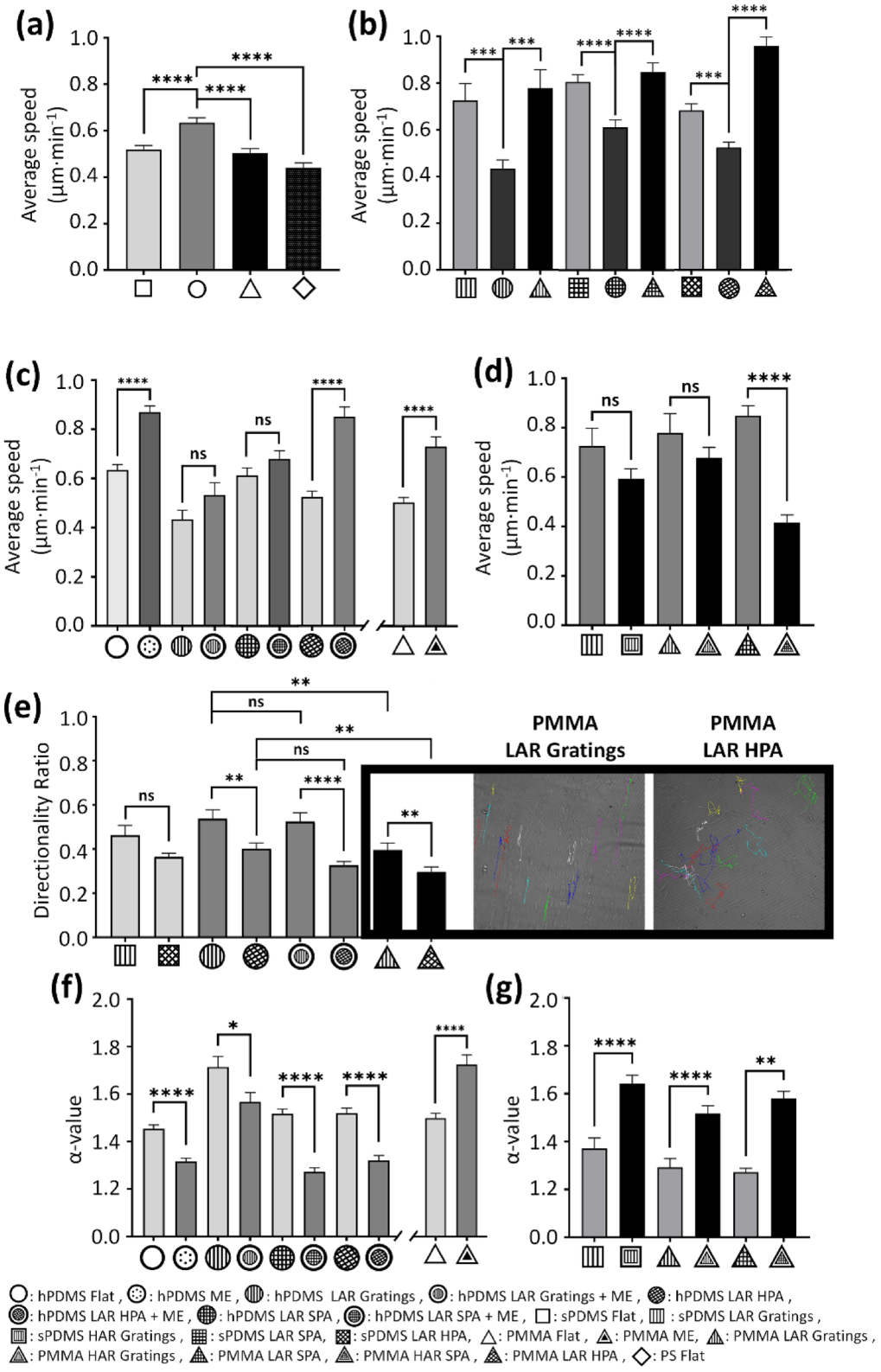

Regarding the influence of the topography, it was seen that micropatterns with either low or high aspect ratio do not have a great impact on the MSCs differentiation, as it can be seen in Figure S7(a) in Supplementary Information. Figure 8(b) compares Alizarin test results for microtextured hPDMS topographies with and without ME nanocones. Enhanced differentiation was observed when the ME nanotextures were patterned, particularly after the 14-day differentiation period.

After this first screening using the Alizarin assay, 21 days was selected as the period for osteogenic-inducing conditions. The differentiation of MSCs towards the osteocyte lineage was further investigated by studying the specific osteogenic biomarkers OCN and OPN. Consistent with the above results, Fig. 8(c) shows shows

◂**Fig. 6**. Comparison of the *average speed* by cell (μm·min^{-1}) of MSCs grown on the different substrates. The plots are grouped comparing parameters of interest: **(a)** polymer (stiffness), **(b)** LAR microstructures, **(c)** presence or not of ME nanostructure, and **(d)** aspect ratio. **(e)***Directionality ratio* of MSCs cultured on the different groups of substrates comparing LAR microtopographies and their homologous hierarchies with some representative cell tracks. *α-values* obtained from the MSCs migration assay on the different substrates comparing **(f)** presence of ME nanostructure also in hierarchical combination and **(g)** aspect ratio. Statistical comparisons were made by means One-way ANOVA followed by Holm-Šidak post-hoc analysis. Significant differences were established by asterisks (* $p<0.05$, ** $p<0.01$, *** $p<0.001$, **** $p<0.0001$) and non-significant (ns) for the corresponding comparisons.

Material	Density (Kg · m^{-3})	E (MPa)	ν (no units)	λ (MPa)	μ (MPa)	Reference
sPDMS	**970**	**2.5**	**0.49**	**0.714**	**0.179**	67,98,99
hPDMS	**970**	**9.0**	--	4.66	0.517	99,100
PMMA	**1185**	**2400**	**0.37**	--	--	101

Table 1. Mechanical parameters for the materials employed to fabricate the topographies simulated by FEM. For soft and hard PDMS, a value of 0.49 was used for the poisson's ratio.

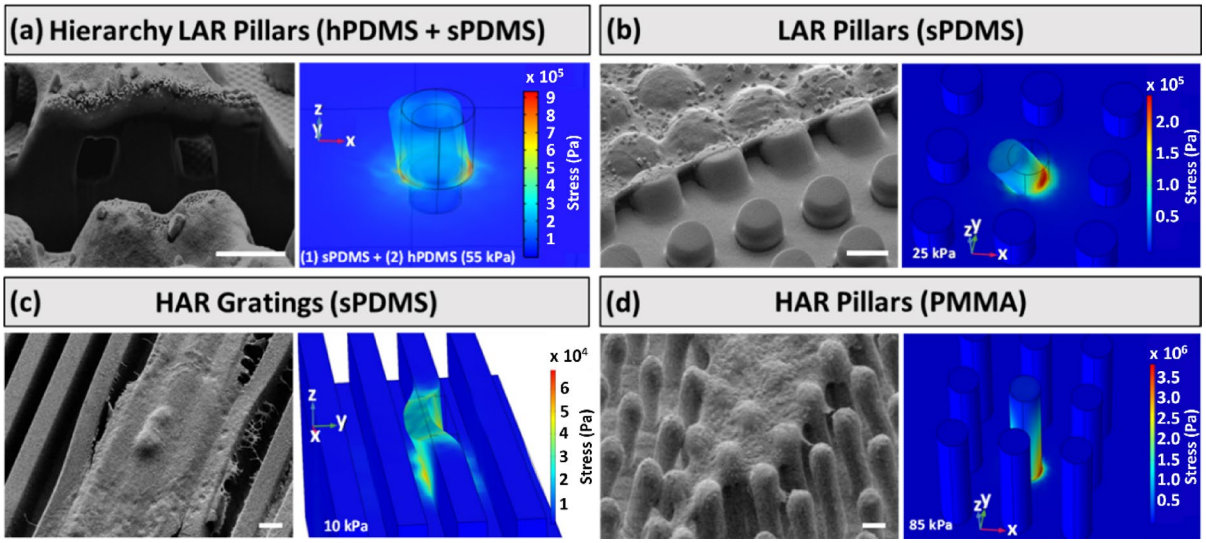

Fig. 7. Comparison of the experimentally observed cellular deflection with the simulated result indicating the induced Von Mises stress distribution under uniaxial force loading (F_A, force per unit area) on different microstructures, including: **(a)** hierarchical micropillars with a bottom layer of sPDMS and a top layer of hPDMS simulated as (1) sPDMS core and hPDMS shell under a F_A = 55 kPa. Focus ion beam ablation was performed to more clearly observe the deflected pillars. **(b)** LAR micropillars fabricated in sPDMS and simulated under a F_A = 25 kPa. **(c)** HAR gratings fabricated in sPDMS and simulated under a load of F_A = 10 kPa. **(d)** HAR micropillars fabricated in PMMA under a lateral load of F_A = 85 kPa. Scale bar: 2 μm.

increased expression of OCN and OPN in the cells grown on the stiffer substrates regardless of the topography. Notably, phenomena such as cell monolayer retraction and cell aggregation were observed, particularly in the softer polymers such as the flat sPDMS and hPDMS substrates, where osteogenic differentiation was also delayed. The observed cellular aggregation may reflect a preservation of stemness, consistent with the well-documented tendency of mesenchymal stem cells (MSCs) to spontaneously form three-dimensional spheroidal structures under appropriate culture conditions[80,81]. See Figures S7, S8, and S9 in the Supplementary Information for visual evidence.

Figure 8(c) also illustrates the effect of the ME nanostructure on the osteogenic differentiation of MSCs. Interestingly, it was found that the expression of the osteogenic markers was lower for the PMMA substrates when patterned with the ME nanostructure compared to its flat counterpart. These results could be a consequence of the reduction of the effective surface stiffness upon nano-/microtexturization[82–84]. Conversely, softer materials such as hPDMS, and nanostructuring with the ME nanocones showed a dramatic increment in the expression of osteogenic marker levels. Implementing the ME patterns in a hierarchical arrangement using hPDMS also resulted in a small, non-significant increment in osteogenic differentiation. These findings align with the Alizarin

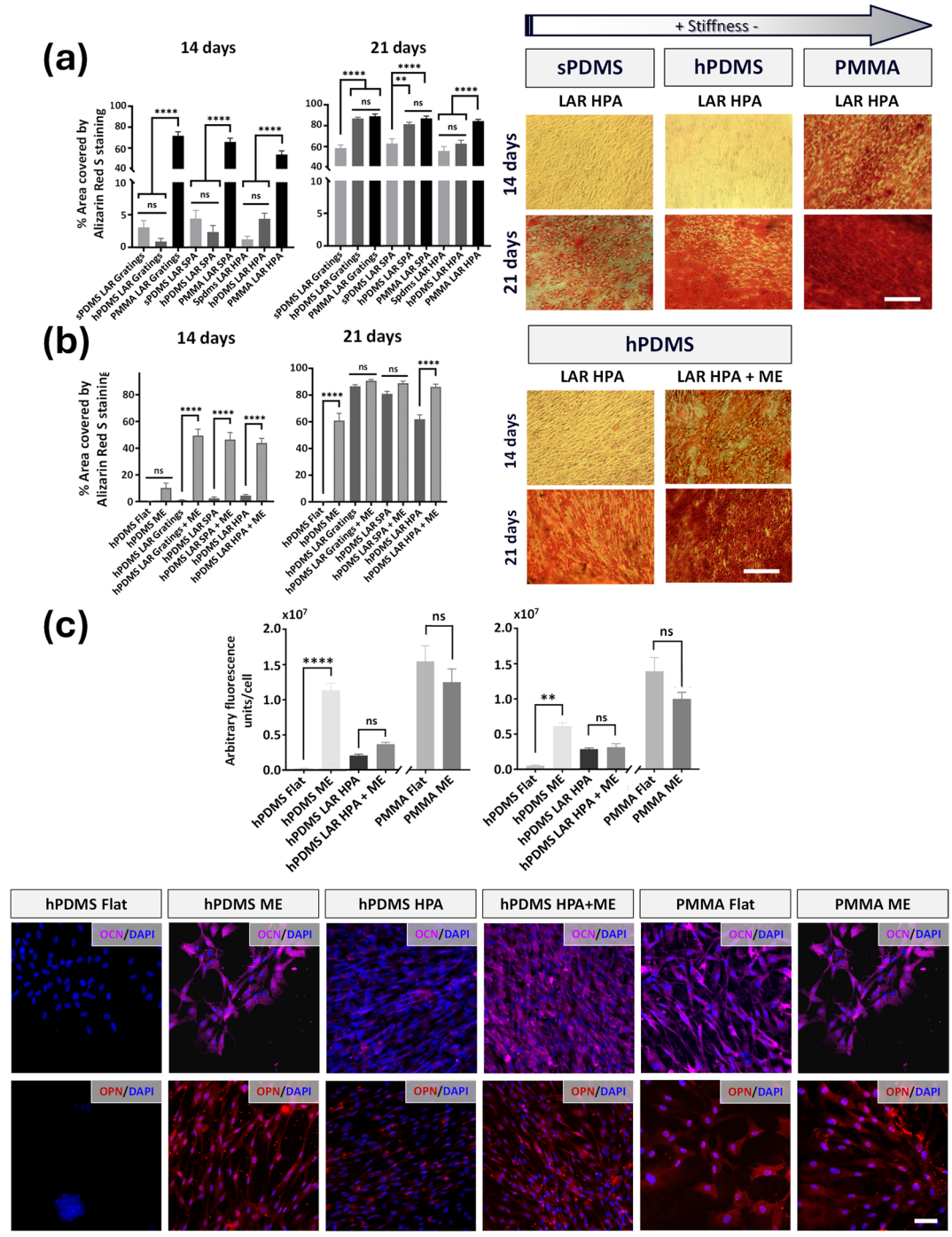

Fig. 8. Percentage of area covered by differentiated MSCs -observed by positive Alizarin Red S staining- after 14 and 21 days of inductive osteogenic culture. Results were obtained for the comparison of **(a)** LAR microtopographies on the different substrate tested, i.e., sPDMS, hPDMS, PMMA, and **(b)** the presence of ME nanotopography, exemplified in both cases with LAR HPA-including microtopography (right). Scale bars: 100 µm. **(c)** OCN and OPN proteins expression in MSCs cultured onto the different substrates for 21 days under inductive osteogenic induction were quantified from immunofluorescence images and expressed as mean ± SE of arbitrary fluorescence units per cell. The results were analyzed to evaluate the influence of polymeric substrate stiffness—specifically hPDMS and PMMA—and the presence of ME nanotopography on cellular osteogenic differentiation, also in hierarchical combination with micron-sized topography (in this case LAR HPA). Representative fluorescence images are shown for OCN (first row) and OPN (second row). One-way ANOVA followed by Holm-Šidak post-hoc test. Significant differences were established by asterisks (* $p < 0.05$, ** $p < 0.01$, *** $p < 0.001$, **** $p < 0.0001$) and non-significant (ns) for the corresponding comparisons. Scale bar: 50 µm.

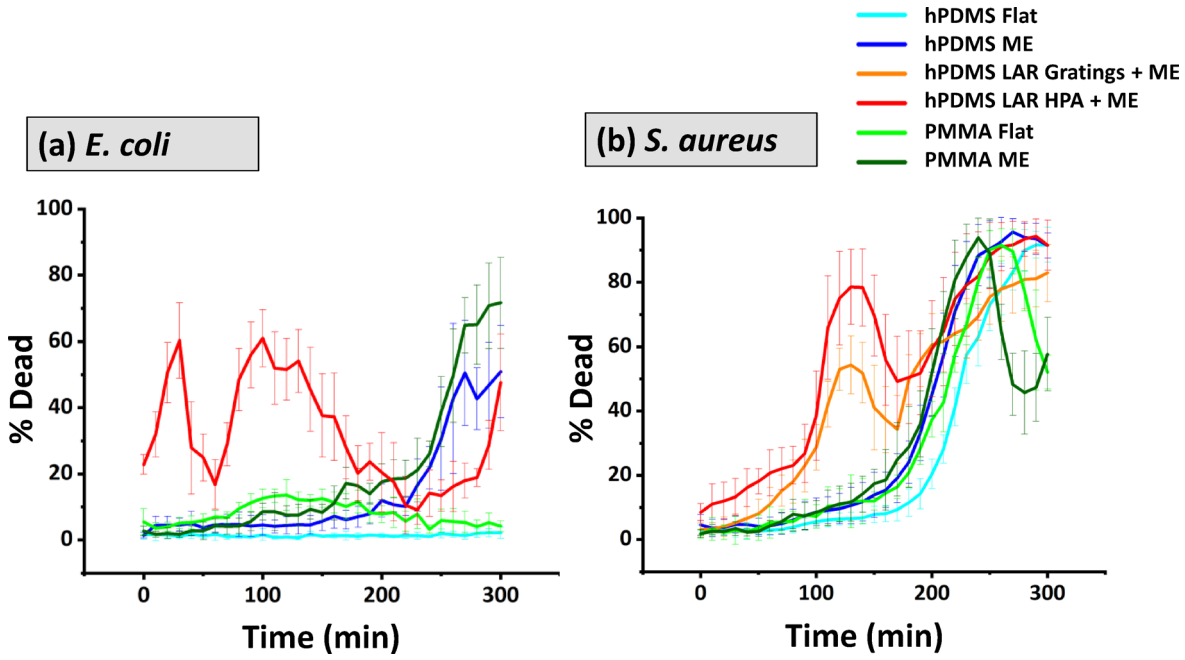

Fig. 9. Bactericidal effect of ME nanostructures monitored using Dead/Live Baclight in **(a)***E. coli* and **(b)***S. aureus* cultured on hPDMS substrate also , including configurations with microscale features such as LAR HPA and LAR gratings, for a duration of 300 min . . The percentage of dead bacteria was calculated every 10 min from fluorescent stained bacteria images. The profiles indicate that MEnanostructures exhibit greater bactericidal effectiveness against *S. aureus* compared to *E. coli*. In the case of the hierarchies, the bactericidal effect of ME nanocones was remarkably earlier but fluctuating over time.

test results. Similarly, introducing microstructures into sPDMS enhances osteogenic differentiation compared to flat surfaces, as particularly evident in Figure S7.

In agreement with previous works, it was found that both micro-/nanotexturization of the surface and stiffness influenced the differentiation of the MSCs[78,7985–88]. Overall, when comparing patterned substrates to their flat counterparts, topographies on softer materials promoted cell differentiation, whereas surface patterning on stiffer materials delayed differentiation. Consequently, cells primarily respond to geometric variations in topography on stiffer materials, while on softer substrates, they react to both stiffness and topographical geometry. This was especially remarkable for the ME nanotopography. These findings are consistent with previous works, which demonstrated similar trends in cellular responses to substrate stiffness[56,89,90], supporting the notion that as stiffness increases, cellular mechanosensing of topographical features is notably reduced, emphasizing the predominant role of stiffness in shaping cellular responses on highly rigid substrates[56]. This finding appears to be linked to the cell-instructive ability of the soft polymer topographies, which demonstrated enhanced osteoinductive properties compared to both smoother controls and stiffer substrates.

Bactericidal effect of the ME nanocones in a hierarchical configuration

The bactericidal capacity of ME nanostructures in hierarchical combination with microscale pillar and grating features was studied by tracking the percentage of dead bacteria for 300 min in different ME nanopatterned materials and their corresponding controls. The experiments were carried out with two different bacterial strains, *E. coli* (gram-negative) and *S. aureus* (gram-positive) to compare the bactericidal effectiveness of both groups of bacteria that bear different bacteria wall characteristics. The bactericidal efficacy for the topographies tested is displayed in Fig. 9. The data was obtained by analyzing the images in Video S2 available as Supplementary Information. The plots obtained indicate that, overall, the bactericidal effect of ME surfaces in a hierarchical configuration becomes be greater than that of ME nanotopography, especially during the initial stages of bacterial attachment, being more effective for *E. coli* than for *S. aureus*, in agreement with previous observations[37,43]. This difference can be attributed to the planktonic nature and more motile of *E. coli*. The findings also indicate that the bactericidal effect takes place at earlier times on the hierarchical ME topographies. This increase is more dramatic for the *E. coli* since it reaches higher dead percentage values at earlier times of the experiment.

Hence, the hierarchical topographies exhibited greater and more rapid bactericidal efficiency, emphasizing their superior antimicrobial performance. This bactericidal enhancement can be attributed to a "gathering effect" induced by the microtopography, where microscale roughness creates sheltered areas that promote bacterial adhesion, ultimately increasing interaction with the ME bactericidal surface.

Additionally, as shown in the plots in Fig. 9, the hierarchical topography exhibited fluctuating cycles in the percentage of dead bacteria, suggesting that the dead bacteria do not remain attached to the surface, but are gradually released. This continuous turnover supports sustained bactericidal activity of the hierarchical topography. This phenomenon may be linked to a recently described 'kill-release' mechanism[91–93]. Therefore,

hierarchical topographies not only improved the bactericidal efficacy but also promote the release of dead bacteria. This prevents the accumulation of bacterial debris on the surface, thereby maintaining sustained bactericidal effectiveness over time.

The bactericidal effect of *E. coli* on the hierarchical topography compared to the micro topography counterpart (LAR HPA + ME) can be seen in the SEM images of Figure S10. These micrographs show the damage and deformation inflicted on the bacteria attached to the ME patterns on the hierarchy compared to that seen on the flat counterparts.

The results, summarized in Tables S4 and S5 in Supplementary Information, signify the complex interplay between surface topography and stiffness in regulating cellular responses. Notably, topographical features can significantly influence the cell behaviour, often exceeding the influence of material stiffness. Moreover, these features can be strategically designed to prevent bacterial colonization, thereby achieving a dual functionality of regulating cell responses while enhancing antibacterial properties. These findings should provide useful insights for designing biomaterial surfaces to improve the biointegration of medical implants.

Conclusions

In conclusion, the micro- and nano-topographies examined in this study, along with their varying degrees of stiffness, played a crucial role in influencing substrate adhesions, ultimately modulating cellular responses to the substrate. The most significant findings indicate that hierarchical topographies with a combination of micro- and nanoscale features influence cell behavior, enhancing osteogenic differentiation, while exhibiting antibacterial properties. This study proposes a multifunctional strategy for improving the biointegration of implantable devices by addressing both host-cell interaction and bacterial infection. Further research could explore the specific mechanotransduction mechanisms underlying these responses and optimize the design of hierarchical topographies for enhanced biointegration and antimicrobial properties.

Methods

Fabrication

Sample description

Different nanofabrication processes and techniques have been used to obtain the desired micro- and nanoscale topographies. The nanometric topography involves ME nanocones with approximately 250 nm diameter at the base and 80 nm on the top, 350 nm high and 250 nm interspacing. LAR microtopographies include pillars with hexagonal and square arrangement and gratings of 2 μm width, 2 μm interspacing, and 2 μm height. Hierarchies merge the same LAR microtopographies with ME nanocones at the top and the bottom of the micrometric features. HAR microtopographies also include pillars with hexagonal and square arrangements and gratings of 2 μm width and 2 μm interspacing, but with 4 μm height in the case of gratings and 10 μm height in the case of pillars. All topographies were fabricated using three polymers: sPDMS, hPDMS and PMMA, except in the case of hierarchies, where the polymer employed for the ME was hPDMS.

ME bioinspired nanocones

The ME nanotopography was fabricated on two different polymer materials following different procedures depending on the nature of the material. The PDMS nanocones were replicated from a nickel master mold (HT-AR-02, Temicon) using the soft-lithography technique. This was performed by depositing two PDMS layers. First, hPDMS was prepared following Schmid et al., 2000 recipe[94]. This layer provides strength to the nanocones and prevents their collapse. The hPDMS layer was first spin-coated onto the master mold at 1000 rpm, 500 rpm · s^{-1}, for 1 min. This layer was pre-cured for 5 min at 80 ℃. Afterwards, sPDMS (Sylgard 184 Silicone Elastomer Kit, Dow Corning) was prepared by mixing crosslinker and precursor (1:10), degassed for 30 min at room temperature and 200 mbar pressure, and then cast over the hPDMS layer. Finally, the hPDMS and sPDMS layers were completely cured at 80℃ overnight before being peeled off from the mold. The PMMA (Evonik Industries AG) ME nanocones were fabricated by thermal nanoimprint lithography (T-NIL) using an EITRE3 Nano Imprint Lithography System (Obducat). For this, the prior PDMS ME substrate was employed as mold. Conditions during the imprint process were 40 bar at 170 ℃ for 300 s. Similarly, PDMS and PMMA polymeric flat substrates were fabricated as control samples following the same procedures as their ME topographical counterparts by applying the same fabrication techniques and protocols but using flat molds.

LAR microtopographies

The LAR microtopographies were fabricated by photolithography (PL). For this, 3-inch silicon wafers (University Wafer, USA) were activated with an oxygen plasma (Tepla 600) at 300 watts and 150 mL · min^{-1} gas flow rate for 5 min, and then Ti-Prime adhesion promoter (MicroChem) was deposited on them, spinning at a speed of 2000 rpm, with an acceleration of 2000 rpm · s^{-1} during 1 min (Spin150i spin coater, Polos). Then, the wafers were baked at 120 ℃ on a hotplate (SUSS MicroTec) for 2 min. Afterwards, a positive photoresist (AZ1512 HS, MicroChem) was deposited by spin-coating at 2000 rpm, 2000 rpm · s^{-1} for 1 min to yield a 2 μm layer thickness. Before the PL process, the wafers were baked for 1 min at 100 ℃ on a hotplate. Finally, the photolithography was performed using a maskless laser writer (Heidelberg DWL66) and developed using the standard AZ351B developer diluted 1:4 in ultrapure water. In this case, AZ1512 being a positive photoresist, the laser-exposed areas were removed when developed obtaining a negative pattern. The lithographed area was typically a square of 25 cm^2 in all cases.

The features obtained after the PL process were replicated by means of soft lithography onto hPDMS according to the abovementioned protocol also used for the ME nanocones fabrication in a hard-soft PDMS bilayer. Similarly, copies on the sPDMS single layer were produced by soft-lithography. The features were also

replicated into PMMA using T-NIL. For features other than gratings, intermediate replication steps were required to optimize the copying of the features to produce a negative template that subsequently led to the positive relief topography, as shown in Figure S11 from Supplementary Information. For this step, an epoxy resin (EPOTEK OG142) was used to replicate the previously obtained PDMS intermediate template through a UV nanoimprint lithography (UV-NIL) step by applying 12 bar at 60 ℃ and exposing it to UV light (80 mW · cm^{-2}) for 120 s. The epoxy resin microtopographies were then replicated on a thermoplastic Intermediate Polymer Stamp (IPS, Obducat) by an additional T-NIL process under conditions of 40 bar at 155 ℃ for 300 s. That IPS was then used as a template to transfer the microstructures by soft lithography on PDMS. Finally, the PDMS substrate was used multiple times as a negative template to reproduce the microfeatures in the PMMA thermoplastic polymer by a T-NIL process. The processing parameters of the NIL processing steps are compiled in Table S2.

Hierarchical microtopographies

The fabrication protocol followed to make hierarchical substrates combining microtopographies and ME nanostructures was based on a previous publication[95]. The process comprises two T-NIL steps and one PL step. In the first T-NIL step, a ME features are imprinted onto a PVDF (Arkema Group KYNAR) thermoplastic thin film under 30 bar at 185 ℃ for 300 s (see Table S2). The thin film was prepared by dissolving PVDF in dimethyl sulfoxide (DMSO) in a concentration of 60 mg · mL^{-1}. Then, silicon wafer was treated with oxygen plasma and coated with Ti-Prime adhesion promoter as described previously. Then the solution of PVDF was spin-coated (2000 rpm, 2000 rpm · s^{-1}, 1 min) onto a 3-in. silicon wafer and baked for 1 min at 100 ℃ on a hotplate to eliminate the solvent before a T-NIL process was performed imprint the ME bottom topography. Afterwards, AZ1512 photoresist was deposited onto the PVDF ME imprinted film by spin-coating (2000 rpm, 2000 rpm · s^{-1}, 1 min) to yield a 2 µm layer thickness. Then, the wafer was baked on the hotplate for 1 min at 100 ℃. Subsequently, the second T-NIL step was carried out on the photoresist to imprint the top ME nanopattern at the conditions shown in Table S2 (100 °C, 30 bar during 180 s). Finally, a PL step was performed using a maskless laser writer as described above. The lithographed area was a square of 25 cm^2.

The formed hierarchic structures were used as molds and replicated using soft lithography using the hard-soft PDMS bilayer, as described above in the section for ME nanotopography substrate fabrication. The fabrication procedure and the resulting substrates are depicted in Figure S12 of the Supplementary Information.

HAR microtopographies

To produce the high aspect ratio (HAR) microfeatures involving pillars and gratings, a commercial silicon mold (LightSmyth Technologies) was used, and a silicon mold was fabricated respectively. For HAR gratings fabrication, maskless PL and dry etching by inductively coupled plasma (ICP) processes were used (see detailed process schematics in Figure S13 of the Supplementary Information).

First, the native oxide layer of the silicon wafers was eliminated by immersing them in a buffered hydrofluoric acid (HF) bath (BOE 7:1, Microchemicals) and then rinsed it with deionized water and dried with nitrogen. Next, the wafers were treated with oxygen plasma and Ti-Prime to promote adhesion of the photoresist. AZ1512 photoresist was then deposited at a speed of 5000 rpm and baked for 1 min at 90 °C, yielding a film of ~1 µm in thickness. PL was performed using the same maskless laser-writer. After the resist was developed, the resulting structures were used as a mask for the next step of etching of the silicon wafers by using the cryogenic process, performed in an Inductively Coupled Plasma Reactive Ion Etching machine (ICP-RIE, Plasmalab 100, Oxford Instruments) with SF_6 and O_2 as process gases. The DC bias voltage employed was 100 V, yielding a selectivity of around 15. The main parameters of this process are listed in Table S3. Once the desired etch depth on the silicon was achieved, the resist mask was removed using acetone, obtaining the master mold.

The silicon molds were treated with an oxygen plasma (300 watts, 150 mL · min^{-1} flow rate, 5 min) to activate the surface. Then, they were exposed to a (1 H, 1 H, 2 H, 2 H-Perfluorodecyltriethoxysilane) (FDTS) atmosphere at 70 ℃ overnight. FTDS acts as an anti-adhesive agent and facilitates the release of the HAR structures during the replication. Finally, the molds were copied employing soft lithography and T-NIL techniques onto sPDMS and PMMA substrates, respectively.

Topography characterization

To evaluate the features' fidelity, scanning electron microscopy (SEM), using a Field Emission Scanning Electron Microscope with Focused Ion Beam (FIB-FSEM Auriga, Carl Zeiss) was employed working on a low voltage (1.0-1.5 kV) and current mode (10 pA) to avoid polymer impairs.

The substrates' wetting behavior was characterized by measuring the static water contact angle (WCA) by means of an optical tensiometer (Attension Theta, Biolin Scientific). For this, 2 µl drops of deionized water were gently placed onto the substrates and static WCAs were calculated by fitting the droplet profile to a Young-Laplace curve. The values provided are average readings from at least three areas in each substrate.

Cell biology experiments

Subculturing procedure

The Mesenchymal Stem Cells (MSCs) employed in this work were ASC52telo, hTERT immortalized adipose-derived (ATCC SCRC-4000, Manassas, USA). The MSCs were cultured using the specific Mesenchymal Stem Cell Growth Kit for Adipose and Umbilical-derived MSCs - Low serum (2% FBS) (ATCC PCS-500040, Manassas, USA) supplemented with gentamicin (PanReac AppliChem #A1492) at a concentration of 10 µg · mL^{-1}. Cell maintenance was performed in T25 flasks, replacing the medium every 2–3 days, and passaging them when reaching approximately 80% confluence as ATCC recommended. MSCs harvesting was performed using TrypLE Express (1x) (Gibco NY, USA, #12604-013) enzymatic treatment. Cells were seeded 5000 cells per cm^2 according to technical specifications and incubated at 37 °C, 95% humidity, and 5% CO_2.

Topographic substrate Preparation for cell culture
Prior to cell culture experiments, the topographic polymeric surfaces were treated to facilitate cell adhesion. Initially, the substrates were punched using a hollow punch tool to manually obtain 18, 12, and 9 mm Ø substrates that fit into 12, 24, and 48 multi-well cell culture plates, respectively. Following, the substrates were fixed to the bottom of each well to prevent them from floating using a tiny drop of sPDMS. The surfaces were cleaned with isopropanol and blow-dried with nitrogen in a clean-room environment to then be exposed to an oxygen plasma (Tepla 600) at 50 watts and 150 mL · min^{-1} gas flow for 1 min for the improvement of wettability of the topographic substrates. Subsequently, the substrates were washed with ethanol 70%, then rinsed with 1x Dulbecco's phosphate-buffered saline (1x DPBS) without Ca^{2+} and Mg^{2+} (Gibco NY, USA, #14190-144) and finally sterilized with UV-light irradiation in a laminar flow cabinet for at least 30 min before the wells were filled with medium and cell culture was performed. The commercial tissue culture plate flat polystyrene (PS) surfaces were used as control.

Immunofluorescence cell staining
The MSCs were cultured for 72 hours at incubating conditions as referred in *Subculturing procedure* and then, the culture medium was removed, and the cells were rinsed with 1x PBS. After that, cells were fixed with 4% paraformaldehyde (4% PFA) (Sigma-Aldrich) for 30 min at 4 ℃ and permeabilized with 0.1% Triton X-100 (Sigma-Aldrich) for 30 min at room temperature. Then, actin cytoskeleton and nucleus staining were performed by incubating with ActinGreen 488 ReadyProbes (Molecular Probes) according to manufacturer technical specifications and 4',6-diamidino-2-phenylindole (DAPI) (Molecular Probes) at 1:100 dilution in 1x PBS for 30 min at room temperature in darkness. Immunofluorescence staining of osteogenic markers, osteopontin (OPN) and osteocalcin (OCN) was carried out by first incubating the cells after osteogenic differentiation with a 1:200 dilution for both mouse anti-OPN (Santa Cruz #sc-21742) and anti-OCN (Santa Cruz #sc-365797) primary antibodies. Subsequently, cells were incubated with 1:500 Alexa-647 rabbit anti-mouse IgG secondary antibody (Molecular Probes) dilution. Both primary and secondary antibody dilutions were made in 0.5% (w/v) Bovine Serum Albumin (BSA) (Sigma-Aldrich) in 1x PBS, and their incubations were carried out for 1 h at 37 ℃ in darkness. DAPI nuclear staining was also conducted together with osteogenic markers immunostaining. After each fixation, permeabilization or incubation step, additional rinsing steps were made with 1x DPBS. Finally, substrates were mounted on microscope slides using Fluoroshield (Sigma-Aldrich) reagent media.

Cell proliferation
The proliferation rates of MSCs cultured on various polymeric micro- and nanotopographies were assessed using a resazurin-based metabolic activity assay, also known as the Alamar Blue assay. A stock solution (10 µg/mL in 1× DPBS) was prepared from resazurin sodium salt powder (Sigma-Aldrich) and sterile-filtered (0.2 µm pore size) to prevent bacterial contamination. For experiments, a working solution was prepared by 1:100 dilution of the stock in culture medium. Cells were incubated with this solution for 4 h at 37 °C in a humidified 5% CO_2 atmosphere. Fluorescence measurements (excitation/emission: 550 nm/590 nm) were collected at designated time points over a 12-day period using a BioTek H4 Hybrid MultiMode Microplate Reader. Following each measurement, substrates were rinsed twice with 1× DPBS and replenished with fresh culture medium.

Cell morphology and spreading
The cell morphology of MSCs grown onto the different substrates was obtained from fluorescent images after nucleus and cytoskeleton staining, taking 10 frames per condition in each of 3 independent experiments. For each condition, >100 cells were recorded in each experiment. Morphological measurements were performed using CellProfiler 3.1.9 software (Broad Institute, USA)[96]. The *MeasureObjectSizeShape* module was used to measure several morphometric parameters. Specifically, three main variables were chosen for the morphological characterization: *Area* (number of pixels covered by a cell), *Circularity* -designed by CellProfiler as *FormFactor*- (calculated as $4\pi[Area/(Perimeter)^2]$, where 1 is a perfectly circular object) and *Eccentricity* (ratio of the distance between the foci of the ellipse and its major axis length, where 0 eccentricity represents a circle whereas 1 is a line), which mathematically describes the elongation. In addition, *Orientation* defined as the angle formed by the x-axis and the major axis of a hypothetical ellipse that outlines the cell and has the same second moments as the region (ranging from −90 to 90 degrees), was also included to estimate the effect that the degree of anisotropy of a particular surface could elicit on cell spreading. Imaging was performed through 20x/0.40 objective using a Leica DMi8 microscope coupled to a monochrome camera Hamamatsu ORCA-Flash 4.0 V3.

Cell spreading over the surface was analyzed by circular statistics in order to obtain an objective parameter for its measure. For this purpose, it was used the CircStat from MATLAB toolbox[97] which allows obtaining descriptive and inferential statistics of directional data. The mean resultant vector $(R = \bar{r})$ of the cell distribution on a surface represents the average of the individual orientation vector components from the n cells in the distribution was computed. The length of the calculated mean resultant vector R ranges from 0 to 1 quantifying the probability of finding a cell along this mean direction on a specific surface where R values closer to 0 mean randomness orientation, while values closer to 1 indicate that all cells were orientated along the same direction. The angle of the mean resultant vector $(\theta = \bar{\alpha})$ indicates this mean direction. The distribution of the *n-cell* orientations and the mean resultant vector were represented as rose plots. Prior to data analysis, minor modifications were made to the original CircStat script, because CellProfiler software only generates data orientations ranging from 90 to −90 degrees in such a way that uniformly distributed data can be misinterpreted as strongly oriented. Therefore, the cell orientation data set (angular data) was extrapolated to obtain the full range of the circumference where the script was run.

Afterwards, a Rayleigh test was performed running the corresponding CircStat script to determine whether each data set had a uniform distribution around the circumference, which is interpreted as a random orientation, or was concentrated around a mean direction, $\bar{\alpha}$. The null hypothesis stated as a population uniformly distributed was rejected when the P-value < 0.05.

Cell migration

Cell migration studies were conducted on MSCs cultured onto the different topographical PDMS and PMMA substrates. Initially, cells were seeded and grown on the substrates for 48 h and the culture medium was renewed prior to the tracking assay. Cell migration data were extracted from time-lapse images using an inverted microscope Axiovert 200 (Zeiss) coupled to a Hamamatsu ORCA-Flash 4.0 LT monochrome camera equipped with a cell incubator chamber. Images were collected using a 10x/0.3 magnification objective for 16 h every 10 min (2–3 positions per replica). A minimum of 10 random cells per location were tracked from at least three locations per substrate. The migratory behavior was analyzed employing the MTrack J plugin from Fiji (NIH) software[98]. Additionally, DiPer Microsoft Excel-macro developed by Gorelik et al.[99] was used to calculate and plot the essential parameters to analyze cell migration in 2D from data previously processed by MTrack J, such as cell trajectories, average speed and mean square displacements (MSDs). The MSD portrays the average square displacements over increasing time intervals between positions of a migration trajectory, relating to the area explored by cells over time. The MSD carries information about both speed and directional persistence during cell movement. The slope of MSD curves linearized using the log (MSD) on the y-axis and the log (time interval) on the x-axis were calculated by using the Slope Analyzer package of OriginPro 2021 version 9.8.0.200 software[100], delivering the α-value. This is a useful parameter for measuring directional persistence; α-values are equal to 1 for randomly moving cells and 2 for cells that move in a perfectly straight manner.

Osteogenesis differentiation

StemPro Osteogenesis Differentiation Kit (Gibco A1007201), supplemented with 10 $\mu g \cdot mL^{-1}$ gentamicin (PanReac AppliChem #A1492), was employed for inducing the differentiation of MSCs towards osteocyte lineage. Before differentiation, MSCs in the low passage (< 8 to 20 passage) were cultured on the different substrates for 24 h in a mesenchymal stem cell growth medium. The next day, this proliferative medium was replaced by an osteogenesis differentiation medium. The culture medium was changed every 3–4 days according to product technical specifications with the differentiation medium for periods of 14–21 days. Subsequently, cells were fixed with 4% PFA for 30 min and rinsed up with 1x DPBS. The cells were then stained with Alizarin Red S (Sigma-Aldrich) by incubating in a 40 mM Alizarin solution in distilled water at pH 4.1 at room temperature for 20 min. Then, the substrates were washed 4 times, for 5 min each time, with distilled water. Stained cells were observed and imaged at 20x/0.70 magnification by using a Leica DMI 3000B microscope coupled to a color Leica DFC310 FX Digital Camera. The images taken were analyzed using the IHC Tool from the Fiji software[101], which allows for precise color detection for subsequent quantification of the percentage of the positively stained area with Alizarin Red corresponding to the calcium deposits by using previously a training set of images. Two random regions of interest (ROIs) from at least five training substrates from each condition were used, while two ROIs from a minimum of ten substrates from each condition were also used for testing. Each set of images was randomly assembled with images from three independent experiments.

Additionally, the expression of the two specific markers of osteogenic differentiation, OCN and OPN were evaluated by immunofluorescence staining as explained above. A minimum of 10 pictures per substrate were taken from the MSCs' immunostained through the 20x/0.40 objective using in this case a Leica DMi8 microscope coupled to a Hamamatsu ORCA-Flash 4.0 V3 monochrome camera. Quantitative results of the expression of the OCN and OPN biomarkers were also obtained using the Fiji software[98]measuring the averaged fluorescence per cell in each image and quantifying the number of cells ($n > 100$ cells per condition) by DAPI staining.

Analysis of cell tractions on topographic features

Simulation of topography Deflection by cell traction forces

The mechanical tractions exerted by the MSCs on the topography were simulated using a Finite Element Model (FEM) using the solid mechanics module of COMSOL Multiphysics version 5.3a software[102]. The materials under study were sPDMS, hPDMS, and PMMA. The FEM simulation was performed for the LAR and HAR pillars in a square arrangement and LAR and HAR gratings (topographical characteristics are given in Table S1).

The topographies were modeled as a mesh. The boundary conditions consisted of all faces of the topographic features being set free except for their base, which was defined as a fixed constraint. On the top face, where force loading was applied, the Boundary Load option was chosen to define the loads implemented in the simulation as force per unit area (F_A). In Figure S14, the top area under load is shown in blue. The load was exerted per single feature, either on a single pillar or on a grating segment defined by a rectangular area of 20×2 µm.

The simulation was performed in two different modes: Linear elastic mode for sPDMS, hPDMS, and PMMA and non-linear hyperelastic mode for sPDMS. Both linear elastic and hyperelastic modes can be seen as the particularization of Hooke's law, $F = k\Delta x$, where F is defined as the force needed to inflict a deformation measured as Δ x distance and k is a constant property of the material (i.e., stiffness). In the first mode, the inputs were Young's modulus, E, expressed in MPa, the Poisson's ratio, ν (dimensionless) and the material density, ρ, expressed in $Kg \cdot m^{-3}$. In the hyperelastic mode, the inputs were the Lamé parameters λ and μ, both expressed in MPa, as well as the material density. These mechanical parameters were obtained from scientific literature (Table 1).

SEM visualization of cell tractions on the topography

To assess surface topography modifications induced by cell traction forces, imaging was performed using a focused ion beam-field emission scanning electron microscope (FIB-FESEM, Auriga, Carl Zeiss). Samples were analyzed in secondary electron detection mode (SE2) with an accelerating voltage of 1.5 kV and a working distance (WD) of 4 mm. For this, after 72 h of MSC culture on the different substrates, the cells were fixed with 4% PFA as mentioned above and then gradually dehydrated incubating with increasing ethanol concentrations: 0, 50, 75, and 100% for 5 min on each step. Later, a 10 nm gold layer was evaporated (e-beam evaporator Evovac, Angstrom Engineering) on them to facilitate charge dissipation during sample imaging. Images were obtained in order to compare with simulated results. To visualize the interaction between the cell and the topography, cross-sectional images of substrates were first obtained after ablation by means of the focused ion beam (FIB-FESEM Auriga, Carl Zeiss).

Microbiological analysis

Bacteria culturing

Two different gram-negative and gram-positive strains, *E. coli* (CECT 516) and *S. aureus* (CECT 240) obtained from the Spanish Type Culture Collection (Colección Española de Cultivos Tipo or CECT, University of Valencia), were used for assessing the bactericidal capacity of the substrates. Initially, bacterial glycerol stocks were cultured overnight in 50 mL of the nutritive broth CECT2 (beef extract 1 g, yeast extract 2 g, peptone 5 g, NaCl 5 g, distilled water 1 L, pH 7.2) at 37 ℃ in an orbital-shaker incubator at 180 rpm. Subsequently, the bacteria suspension was diluted 1:100 in the culture broth and grown until reaching optical density $OD_{600} = 0.2$. These pre-cultures were seeded onto the topographies for evaluating their bactericidal effect in bacterial death monitoring tests.

Bacterial attachment

The prepared topographic substrates were placed into 24-well multi-well plates. For this, 14 mm Ø substrates were punched out and fixed at the bottom of each well using a drop of sPDMS and curing it to prevent floating upon the addition of the bacterial suspension. Then 1 mL of bacterial suspension was added per well and incubated for 5 h at 37 ℃ under static conditions. After the incubation period, substrates were rinsed with 1x PBS (Biowest) and then fixed with 4% PFA (Sigma-Aldrich) for 20 min. Subsequently, the substrates were gradually dehydrated, incubating them with increasing ethanol concentrations as previously described. Afterwards, substrates were inspected and imaged by SEM (FIB-FSEM Auriga, Carl Zeiss), working at a low voltage (1.0-1.5 kV) and current (10 pA) mode to minimize polymer and bacteria damage.

Bactericidal efficiency evaluation

The bactericidal efficacy of ME nanocones, both alone and in hierarchical combination fabricated in hPDMS, was evaluated in comparison to the flat control using the Live/Dead Baclight Viability Kit (Molecular Probes). This kit contains two fluorescence dyes, Syto9 and propidium iodide (PI), that differentially stain live and dead bacteria, respectively. For these experiments, 9 mm Ø manually punched substrates were placed and glued to the bottom of the wells of Ibidi µ-slide 8-well plates (Ibidi GmbH, Germany) using a drop of sPDMS. Once the well plates were prepared, substrates were sterilized by rinsing them with ethanol 70% and 1x PBS (Biowest), and finally exposing them with UV light in laminar flow cabinet for 30 min. Bacteria precultures ($OD_{600} = 0.2$) were then incubated with 0.13 µL of each of the dyes, Syto9 and PI, per 1 mL of bacterial suspension for 15 min at room temperature in darkness. Following, 100 µL of this bacterial suspension was used as inoculum and deposited in each well. Images of the stained bacteria were taken through a 20x/0.4 objective at a suitable wavelength every 10 min for a 5 h time-lapse. Imaging was performed using an inverted Leica DMI6000B epifluorescence microscope coupled to an ORCA-R2 monochrome digital camera and equipped with a thermally controlled stage at 37 ℃. The images collected were binarized and the pixels of the stained areas were measured using the Fiji software (NIH, Bethesda, MD, USA). The percentage of bacteria death was calculated from the areas stained with Syto9 corresponding to live bacteria and PI corresponding to dead bacteria. The bactericidal efficacy of the substrates is given as the ratio of (Pixel area of *Dead bacteria*/ Pixel are of *Total bacteria*) x 100, where total bacteria is the sum of alive and dead bacteria.

Statistical analysis

Each experiment was performed in triplicate and included at least three experimental subjects per condition to assess the reproducibility unless otherwise stated. The ROUT method was chosen to clean the data by detecting outliers with a maximum of 1% False Discovery Rate (FDR), that is, false outliers' rate (Q = 1%). Subsequently, *One-way ANOVA* statistical analysis followed by *Holm-Šídák* post-hoc test for multiple comparisons were performed. The results were represented as mean ± standard error of the mean (Mean ± SE). Data preprocessing, plotting and statistical analysis were conducted using GraphPad Prism 8.0.1 version[103]. Data were considered statistically significant at p value < 0.05 (*), p value < 0.01 (**), p value < 0.01 (***) and p value < 0.0001 (****).

Data availability

Sequence data that support the findings of this study have been deposited in the Institutional Repository of IMDEA Nanociencia. https://nanociencia.imdea.org/repository.

Received: 11 October 2024; Accepted: 20 June 2025
Published online: 14 July 2025

References

1. Mao, A. S. & Mooney, D. J. Regenerative medicine: Current therapies and future directions. *Proceedings of the National Academy of Sciences* 112, 14452–14459 (2015).
2. Corsi, K. A., Schwarz, E. M., Mooney, D. J. & Huard, J. Regenerative medicine in orthopaedic surgery. *J. Orthop. Res.* **25**, 1261–1268 (2007).
3. Li, B. & Webster, T. J. Bacteria antibiotic resistance: new challenges and opportunities for implant-associated orthopedic infections. *J. Orthop. Research*®. **36**, 22–32 (2018).
4. Arciola, C. R., Campoccia, D., Ehrlich, G. D. & Montanaro, L. Biofilm-based implant infections in orthopaedics. *Biofilm-based Healthcare-associated Infections: I* **830**, 29–46 (2015).
5. Victor, S. P., Pillai, C. & Sharma, C. P. in *Biointegration of Medical Implant Materials* 1–16Elsevier, (2020).
6. Kashi, A. & Saha, S. in *Biointegration of Medical Implant Materials* 407–432Elsevier, (2020).
7. Gristina, A. G., Naylor, P. & Myrvik, Q. Infections from biomaterials and implants: a race for the surface. *Med. Prog Technol.* **14**, 205–224 (1988).
8. Di Domenico, E. G., Oliva, A. & Guembe, M. The current knowledge on the pathogenesis of tissue and medical device-related biofilm infections. *Microorganisms* **10**, 1259 (2022).
9. Davies, D. Understanding biofilm resistance to antibacterial agents. *Nat. Rev. Drug Discovery*. **2**, 114–122 (2003).
10. Nguyen, S. H., Webb, H. K., Crawford, R. J. & Ivanova, E. P. Natural antibacterial surfaces. *Antibacterial Surfaces*, 9–26 (2015).
11. Campoccia, D., Montanaro, L. & Arciola, C. R. The significance of infection related to orthopedic devices and issues of antibiotic resistance. *Biomaterials* **27**, 2331–2339 (2006).
12. Dalby, M. J. et al. The control of human mesenchymal cell differentiation using nanoscale symmetry and disorder. *Nat. Mater.* **6**, 997–1003 (2007).
13. Bettinger, C. J., Langer, R. & Borenstein, J. T. Engineering substrate topography at the micro-and nanoscale to control cell function. *Angew. Chem. Int. Ed.* **48**, 5406–5415 (2009).
14. Viela, F., Granados, D., Ayuso-Sacido, A. & Rodríguez, I. Biomechanical cell regulation by high aspect ratio nanoimprinted pillars. *Adv. Funct. Mater.* **26**, 5599–5609 (2016).
15. Abagnale, G. et al. Surface topography guides morphology and Spatial patterning of induced pluripotent stem cell colonies. *Stem Cell. Rep.* **9**, 654–666 (2017).
16. Lim, J. Y. et al. The regulation of integrin-mediated osteoblast focal adhesion and focal adhesion kinase expression by nanoscale topography. *Biomaterials* **28**, 1787–1797 (2007).
17. Biggs, M. J. et al. The use of nanoscale topography to modulate the dynamics of adhesion formation in primary osteoblasts and ERK/MAPK signalling in STRO-1 enriched skeletal stem cells. *Biomaterials* **30**, 5094–5103 (2009).
18. Yim, E. K., Darling, E. M., Kulangara, K., Guilak, F. & Leong, K. W. Nanotopography-induced changes in focal adhesions, cytoskeletal organization, and mechanical properties of human mesenchymal stem cells. *Biomaterials* **31**, 1299–1306 (2010).
19. Seo, C. H., Furukawa, K., Montagne, K., Jeong, H. & Ushida, T. The effect of substrate microtopography on focal adhesion maturation and actin organization via the rhoa/rock pathway. *Biomaterials* **32**, 9568–9575 (2011).
20. Teo, B. K. K. et al. Nanotopography modulates mechanotransduction of stem cells and induces differentiation through focal adhesion kinase. *ACS Nano*. **7**, 4785–4798 (2013).
21. Burridge, K. Focal adhesions: a personal perspective on a half century of progress. *FEBS J.* **284**, 3355–3361 (2017).
22. Kumar, S. Stiffness does matter. *Nat. Mater.* **13**, 918–920 (2014).
23. Lv, H. et al. Mechanism of regulation of stem cell differentiation by matrix stiffness. *Stem Cell Res. Ther.* **6**, 1–11 (2015).
24. Seewaldt, V. ECM stiffness paves the way for tumor cells. *Nat. Med.* **20**, 332–333 (2014).
25. Rianna, C. & Radmacher, M. Influence of microenvironment topography and stiffness on the mechanics and motility of normal and cancer renal cells. *Nanoscale* **9**, 11222–11230 (2017).
26. McNamara, L. E. et al. Nanotopographical control of stem cell differentiation. *J. Tissue Eng.* **1**, 120623 (2010).
27. Donnelly, H., Salmeron-Sanchez, M. & Dalby, M. J. Designing stem cell niches for differentiation and self-renewal. *J. Royal Soc. Interface*. **15**, 20180388 (2018).
28. Maxson, S., Lopez, E. A., Yoo, D., Danilkovitch-Miagkova, A. & LeRoux, M. A. Concise review: role of mesenchymal stem cells in wound repair. *Stem Cells Translational Med.* **1**, 142–149 (2012).
29. Balaji, S., Keswani, S. G. & Crombleholme, T. M. The role of mesenchymal stem cells in the regenerative wound healing phenotype. *Adv. Wound Care*. **1**, 159–165 (2012).
30. McMurray, R. J. et al. Nanoscale surfaces for the long-term maintenance of mesenchymal stem cell phenotype and multipotency. *Nat. Mater.* **10**, 637–644 (2011).
31. Pedrosa, C. R. et al. Controlled nanoscale topographies for osteogenic differentiation of mesenchymal stem cells. *ACS Appl. Mater. Interfaces*. **11**, 8858–8866 (2019).
32. Zhang, B., Huang, J. & Narayan, R. *In Nanostructured Biomaterials for Regenerative Medicine*47–80 (Elsevier, 2020).
33. Jaggessar, A., Shahali, H., Mathew, A. & Yarlagadda, P. K. Bio-mimicking nano and micro-structured surface fabrication for antibacterial properties in medical implants. *J. Nanobiotechnol.* **15**, 1–20 (2017).
34. Neinhuis, C. & Barthlott, W. Characterization and distribution of water-repellent, self-cleaning plant surfaces. *Ann. Botany*. **79**, 667–677 (1997).
35. Zhang, X., Wang, L. & Levänen, E. Superhydrophobic surfaces for the reduction of bacterial adhesion. *RSC Adv.* **3**, 12003–12020 (2013).
36. Han, Z. et al. Long-term durability of superhydrophobic properties of butterfly wing scales after continuous contact with water. *Colloids Surf. Physicochem Eng. Aspects*. **518**, 139–144 (2017).
37. Viela, F., Navarro-Baena, I., Hernández, J. J., Osorio, M. R. & Rodríguez, I. Moth-eye mimetic cytocompatible bactericidal nanotopography: A convergent design. *Bioinspir. Biomim.* **13**, 026011 (2018).
38. Mainwaring, D. E. et al. The nature of inherent bactericidal activity: insights from the nanotopology of three species of dragonfly. *Nanoscale* **8**, 6527–6534 (2016).
39. Truong, V. K. et al. The susceptibility of Staphylococcus aureus CIP 65.8 and Pseudomonas aeruginosa ATCC 9721 cells to the bactericidal action of nanostructured Calopteryx haemorrhoidalis damselfly wing surfaces. *Appl. Microbiol. Biotechnol.* **101**, 4683–4690 (2017).
40. Hasan, J. et al. Selective bactericidal activity of nanopatterned superhydrophobic cicada psaltoda claripennis wing surfaces. *Appl. Microbiol. Biotechnol.* **97**, 9257–9262 (2013).
41. Román-Kustas, J. et al. Molecular and topographical organization: influence on cicada wing wettability and bactericidal properties. *Adv. Mater. Interfaces*. **7**, 2000112 (2020).
42. Linklater, D. P. et al. Mechano-bactericidal actions of nanostructured surfaces. *Nat. Rev. Microbiol.* **19**, 8–22 (2021).
43. Alameda, M. T., Osorio, M. R., Pedraz, P. & Rodríguez, I. Mechano-Dynamic analysis of the bactericidal activity of bioinspired Moth-Eye nanopatterned surfaces. *Adv. Mater. Interfaces*. **9**, 2200608 (2022).
44. Pham, V. T. et al. Race for the surface: eukaryotic cells can win. *ACS Appl. Mater. Interfaces*. **8**, 22025–22031 (2016).
45. Liu, H. et al. Mechanisms of hierarchical topographies tuning Bacteria and cell biological responses to the surfaces of pure titanium and Cu-Bearing titanium alloy. *ACS Appl. Mater. Interfaces*. **14**, 19226–19240 (2022).
46. Cun, X. & Hosta-Rigau, L. Topography: a biophysical approach to direct the fate of mesenchymal stem cells in tissue engineering applications. *Nanomaterials* **10**, 2070 (2020).

47. Bonde, S. et al. Exploring arrays of vertical one-dimensional nanostructures for cellular investigations. *Nanotechnology* **25**, 362001 (2014).
48. Schmidt, D. R., Waldeck, H. & Kao, W. J. Protein adsorption to biomaterials. *Biological interactions on materials surfaces: Understanding and controlling protein, cell, and tissue responses*, 1–18 (2009).
49. Ramsey, W. S., Hertl, W., Nowlan, E. D. & Binkowski, N. J. Surface treatments and cell attachment. *Vitro* **20**, 802–808 (1984).
50. Grace, J. M. & Gerenser, L. J. Plasma treatment of polymers. *J. Dispersion Sci. Technol.* **24**, 305–341 (2003).
51. Recek, N. Biocompatibility of plasma-treated polymeric implants. *Materials* **12**, 240 (2019).
52. Beijer, N. R. et al. Dynamic adaptation of mesenchymal stem cell physiology upon exposure to surface micropatterns. *Sci. Rep.* **9**, 9099 (2019).
53. Colley, H. E., Mishra, G., Scutt, A. M. & McArthur, S. L. Plasma polymer coatings to support mesenchymal stem cell adhesion, growth and differentiation on variable stiffness silicone elastomers. *Plasma Processes Polym.* **6**, 831–839 (2009).
54. Rosales-Leal, J. I. et al. Effect of roughness, wettability and morphology of engineered titanium surfaces on osteoblast-like cell adhesion. *Colloids Surf. Physicochem Eng. Aspects*. **365**, 222–229 (2010).
55. Majhy, B., Priyadarshini, P. & Sen, A. K. Effect of surface energy and roughness on cell adhesion and growth–facile surface modification for enhanced cell culture. *RSC Adv.* **11**, 15467–15476 (2021).
56. Yang, Y., Wang, K., Gu, X. & Leong, K. W. Biophysical regulation of cell behavior—cross talk between substrate stiffness and nanotopography. *Engineering* **3**, 36–54 (2017).
57. Wolfenson, H., Yang, B. & Sheetz, M. P. Steps in mechanotransduction pathways that control cell morphology. *Annu. Rev. Physiol.* **81**, 585–605 (2019).
58. Kuo, C. W., Chueh, D. & Chen, P. Investigation of size–dependent cell adhesion on nanostructured interfaces. *J. Nanobiotechnol.* **12**, 1–10 (2014).
59. Chien, F., Dai, Y., Kuo, C. W. & Chen, P. Flexible nanopillars to regulate cell adhesion and movement. *Nanotechnology* **27**, 475101 (2016).
60. Ray, A. et al. Anisotropic forces from spatially constrained focal adhesions mediate contact guidance directed cell migration. *Nat. Commun.* **8**, 14923 (2017).
61. Leclech, C. & Barakat, A. I. Is there a universal mechanism of cell alignment in response to substrate topography? *Cytoskeleton* **78**, 284–292 (2021).
62. Zhang, W., Choi, D. S., Nguyen, Y. H., Chang, J. & Qin, L. Studying cancer stem cell dynamics on PDMS surfaces for microfluidics device design. *Sci. Rep.* **3**, 2332 (2013).
63. Blatchley, M. R. & Anseth, K. S. Middle-out methods for Spatiotemporal tissue engineering of organoids. *Nat. Reviews Bioeng.* **1**, 329–345 (2023).
64. Tenreiro, M. F. et al. Advancing organoid design through co-emergence, assembly, and bioengineering. *Trends Biotechnol.* **41**, 923–938 (2023).
65. Peyton, S. R. & Putnam, A. J. Extracellular matrix rigidity governs smooth muscle cell motility in a biphasic fashion. *J. Cell. Physiol.* **204**, 198–209 (2005).
66. Bangasser, B. L. et al. Shifting the optimal stiffness for cell migration. *Nat. Commun.* **8**, 15313 (2017).
67. Pathak, A. Modeling and predictions of biphasic mechanosensitive cell migration altered by cell-intrinsic properties and matrix confinement. *Phys. Biol.* **15**, 065001 (2018).
68. Reversat, A. et al. Cellular locomotion using environmental topography. *Nature* **582**, 582–585 (2020).
69. Cavalcanti-Adam, E. A. et al. Cell spreading and focal adhesion dynamics are regulated by spacing of integrin ligands. *Biophys. J.* **92**, 2964–2974 (2007).
70. Webb, D. J., Parsons, J. T. & Horwitz, A. F. Adhesion assembly, disassembly and turnover in migrating cells–over and over and over again. *Nat. Cell. Biol.* **4**, E97–E100 (2002).
71. Liang, E. I., Mah, E. J., Yee, A. F. & Digman, M. A. Correlation of focal adhesion assembly and disassembly with cell migration on nanotopography. *Integr. Biology*. **9**, 145–155 (2017).
72. Crouch, A. S., Miller, D., Luebke, K. J. & Hu, W. Correlation of anisotropic cell behaviors with topographic aspect ratio. *Biomaterials* **30**, 1560–1567 (2009).
73. Jeon, H., Hidai, H., Hwang, D. J., Healy, K. E. & Grigoropoulos, C. P. The effect of micronscale anisotropic cross patterns on fibroblast migration. *Biomaterials* **31**, 4286–4295 (2010).
74. Schoen, I., Hu, W., Klotzsch, E. & Vogel, V. Probing cellular traction forces by micropillar arrays: contribution of substrate warping to pillar Deflection. *Nano Lett.* **10**, 1823–1830 (2010).
75. Tan, J. L. et al. Cells lying on a bed of microneedles: an approach to isolate mechanical force. *Proceedings of the National Academy of Sciences* 100, 1484–1489 (2003).
76. Johari, S. & &Shyan, L. Y. *Stress-strain relationship of PDMS micropillar for force measurement application*EPJ Web of Conferences Ser. 162, EDP Sciences, (2017).
77. Trichet, L. et al. Evidence of a large-scale mechanosensing mechanism for cellular adaptation to substrate stiffness. *Proc. Natl. Acad. Sci.* **109**, 6933–6938 (2012).
78. Witkowska-Zimny, M. et al. Effect of substrate stiffness on the osteogenic differentiation of bone marrow stem cells and bone-derived cells. *Cell. Biol. Int.* **37**, 608–616 (2013).
79. Hsieh, W. et al. Matrix dimensionality and stiffness cooperatively regulate osteogenesis of mesenchymal stromal cells. *Acta Biomater.* **32**, 210–222 (2016).
80. Bartosh, T. et al. (ed, J.) Aggregation of human mesenchymal stromal cells (MSCs) into 3D spheroids enhances their antiinflammatory properties. *Proc. Natl. Acad. Sci.* **107** 13724–13729 (2010).
81. Jiang, N. et al. Regulation mechanisms and maintenance strategies of stemness in mesenchymal stem cells. *Stem Cell. Reviews Rep.* **20**, 455–483 (2024).
82. Bucaro, M. A., Vasquez, Y., Hatton, B. D. & Aizenberg, J. Fine-tuning the degree of stem cell polarization and alignment on ordered arrays of high-aspect-ratio nanopillars. *ACS Nano*. **6**, 6222–6230 (2012).
83. Fu, J. et al. Mechanical regulation of cell function with geometrically modulated elastomeric substrates. *Nat. Methods*. **7**, 733–736 (2010).
84. Janbaz, S., Weinans, H. & Zadpoor, A. A. Geometry-based control of instability patterns in cellular soft matter. *RSC Adv.* **6**, 20431–20436 (2016).
85. Watari, S. et al. Modulation of osteogenic differentiation in hMSCs cells by submicron topographically-patterned ridges and grooves. *Biomaterials* **33**, 128–136 (2012).
86. Yang, W. et al. Surface topography of hydroxyapatite promotes osteogenic differentiation of human bone marrow mesenchymal stem cells. *Mater. Sci. Engineering: C*. **60**, 45–53 (2016).
87. Sun, M. et al. Extracellular matrix stiffness controls osteogenic differentiation of mesenchymal stem cells mediated by integrin α5. *Stem Cell Res. Ther.* **9**, 1–13 (2018).
88. Yang, L. et al. Biomimetic multiscale hierarchical topography enhances osteogenic differentiation of human mesenchymal stem cells. *Adv. Mater. Interfaces*. **7**, 2000385 (2020).
89. Weng, S. & Fu, J. Synergistic regulation of cell function by matrix rigidity and adhesive pattern. *Biomaterials* **32**, 9584–9593 (2011).
90. Feld, L. et al. Cellular contractile forces are nonmechanosensitive. *Sci. Adv.* **6**, eaaz6997 (2020).

91. Wei, T., Tang, Z., Yu, Q. & Chen, H. Smart antibacterial surfaces with switchable bacteria-killing and bacteria-releasing capabilities. *ACS Appl. Mater. Interfaces*. **9**, 37511–37523 (2017).
92. Nguyen, D. H. et al. The idiosyncratic self-cleaning cycle of bacteria on regularly arrayed mechano-bactericidal nanostructures. *Nanoscale* **11**, 16455–16462 (2019).
93. Yi, Y. et al. Bioinspired nanopillar surface for switchable mechano-bactericidal and releasing actions. *J. Hazard. Mater.* **432**, 128685 (2022).
94. Schmid, H. & Michel, B. Siloxane polymers for high-resolution, high-accuracy soft lithography. *Macromolecules* **33**, 3042–3049 (2000).
95. Alameda, M. T., Osorio, M. R., Hernández, J. J. & Rodríguez, I. Multilevel hierarchical topographies by combined photolithography and Nanoimprinting processes to create surfaces with controlled wetting. *ACS Appl. Nano Mater.* **2**, 4727–4733 (2019).
96. Carpenter, A. E. et al. CellProfiler: image analysis software for identifying and quantifying cell phenotypes. *Genome Biol.* **7**, 1–11 (2006).
97. Berens, P. CircStat: a MATLAB toolbox for circular statistics. *J. Stat. Softw.* **31**, 1–21 (2009).
98. Schindelin, J. et al. Fiji: an open-source platform for biological-image analysis. *Nat. Methods*. **9**, 676–682 (2012).
99. Gorelik, R. & Gautreau, A. Quantitative and unbiased analysis of directional persistence in cell migration. *Nat. Protoc.* **9**, 1931–1943 (2014).
100. OriginPro, N. *OriginLab Corporation, Northampton, MA, USA* (2021).
101. Shu, J., Dolman, G. E., Duan, J., Qiu, G. & Ilyas, M. Statistical colour models: an automated digital image analysis method for quantification of histological biomarkers. *Biomed. Eng. Online*. **15**, 1–16 (2016).
102. Comsol, A. B. COMSOL Multiphysics® Reference Manual, v. 5.4. *COMSOL AB: Stockholm, Sweden* (2018).
103. GraphPad, P. Version 8.0.1 for Windows. GraphPad Prism, Inc. *GraphPad Prism Inc., San Diego, California USA* (2018).

Acknowledgements

We gratefully acknowledge financial support from the Spanish Ministry of Science and Innovation (MICINN) under the project REGINNA (PID2020-120202RB-I00) and the project NanoScell (PDC2021-121515-I00). IMDEA Nanociencia receives support from the 'Severo Ochoa' Programme for Centres of Excellence in R&D (MICINN Grant no: CEX2020-001039-S).

Author contributions

M. T. A. designed and realized all microbiological and cell biology experiments, conceived, and performed the experimental measurements, analyzed the data, fabricated the polymeric surfaces and wrote the original manuscript. M. R. O. conceived and contributed to the fabri-cation process, performed the SEM imaging, conceived and analyzed the FEM simulation, and participated in the manuscript writing. J. J. H., designed and contributed to the fabrication process. I. R. conceptualized and supervised the research work, funding acquisition, manuscript writing review and editing. All authors contributed to the discussion and analysis of the results presented and reviewed the manuscript.

Funding

Spanish Ministry of Science and Innovation (MICINN) under the project REGINNA (PID2020-120202RB-I00) and project NanoScell (PDC2021-121515-I00). IMDEA Nanociencia support from the 'Severo Ochoa' Programme for Centres of Excellence in R&D (MICINN Grant no: CEX2020-001039-S).

Declarations

Competing interests

The authors declare no competing interests.

Additional information

Supplementary Information The online version contains supplementary material available at https://doi.org/10.1038/s41598-025-08415-2.

Correspondence and requests for materials should be addressed to M.T.A. or I.R.